Direct conversion of carbon dioxide into liquid fuels and chemicals by coupling green hydrogen at high temperature

Yubing Li [a],[1], Lei Zeng [a],[1], Ge Pang [a], Xueer Wei [a], Mengheng Wang [a],[*], Kang Cheng [a],[b],[*], Jincan Kang [a], José M. Serra [c], Qinghong Zhang [a],[*], Ye Wang [a],[b]

[a] State Key Laboratory of Physical Chemistry of Solid Surfaces, Collaborative Innovation Center of Chemistry for Energy Materials, College of Chemistry and Chemical Engineering, Xiamen University, Xiamen 361005, China
[b] Innovation Laboratory for Sciences and Technologies of Energy Materials of Fujian Province (IKKEM), Xiamen University, Xiamen 361005, China
[c] Instituto de Tecnología Química, Consejo Superior de Investigaciones Científicas-Universitat Politècnica de València, 46022 Valencia, Spain

ARTICLE INFO

ABSTRACT

The chemical conversion of CO_2 into hydrocarbon fuels and chemicals using green hydrogen not only utilizes abundant CO_2 as a carbon feedstock but also enables the storage of hydrogen. Herein, we investigate the direct hydrogenation of CO_2 to gasoline and olefins over a series of bifunctional iron-zeolite tandem catalysts operated at high temperatures (> 300 ℃). This process may efficiently utilize CO_2 discharged from industrial combustion and green H_2 produced by solid oxide electrolytic cells (SOEC). The optimized FeMnK+H-ZSM-5 catalyst offers a 70% selectivity of C_5-C_{11} range hydrocarbons together with a 17% selectivity of C_2-C_4 lower olefins at 320 ℃. The CO_2 conversion levels and the aromatics contents could be greatly enhanced as the temperature increases from 320 ℃ to 400 ℃. The hydrocarbon distribution is mainly determined by the micropore size of the zeolites. The dynamic evolution of bifunctional catalysts and its impact on bifunctional catalysis was systematically investigated.

1. Introduction

The concentration of CO_2, the primary greenhouse gas, reaches 417 ppm in 2022, more than 50% higher than pre-industrial levels. To fight against climate change, it is essential to reduce CO_2 emissions and utilize CO_2 as a feedstock or resource, which may bring a significant challenge to traditional fossil-based and carbon-intensive industries [1–3]. Nowadays, carbon capture, utilization, and storage (CCUS) is one of the promising technologies that can contribute to net-zero emissions and provide carbon resources for producing hydrocarbon fuels and chemicals [4–7]. With the fast development of green electricity and H_2 from renewable energy sources (e.g. wind, hydraulic power, biomass, and solar), the chemical conversion of CO_2 becomes practicable and promising (Fig. 1) [8–10]. Therefore, the conversion of CO_2 to fuels and chemicals by green energy attracts worldwide attention because it can not only consume the abundant CO_2 but also enables the storage of H_2 [11–13].

The catalytic conversion of CO_2 into hydrocarbon fuels and

chemicals can be achieved through electrocatalysis using green electricity directly and thermal catalysis using green H_2 (Fig. 1). Electrocatalysis mainly produces C_1 or C_2 products (e.g., CO, formic acid, ethylene, and ethanol) with high Faraday efficiency but inferior product yields [14–16]. While thermal catalysis is more suitable for the production of liquid fuels with multiple carbons (e.g. gasoline, diesel, jet fuel, and aromatics) and is applicable to mature industrial technology [17–21]. Green H_2 can be produced by electrolyzing water in various types of electrolytic cells using zero-carbon electricity. Particularly, the solid oxide electrolytic cells (SOEC), uniquely characterized by high-temperature water electrolysis or steam electrolysis (> 500 ℃), provide higher stack electrical efficiency ($> 90\%$) and energy efficiency ($> 80\%$) [22,23]. Considering the CO_2 discharged from industries is also high-temperature [24], the co-conversion of H_2 from SOEC and CO_2 from industry enables direct and efficient CO_2 transformation to a great extent without storage and transportation (Fig. 1). From the catalyst aspect, those can operate at high temperatures and allow the control of product distribution is highly desired, which can increase the utilization

---

* Corresponding authors at: State Key Laboratory of Physical Chemistry of Solid Surfaces, Collaborative Innovation Center of Chemistry for Energy Materials, College of Chemistry and Chemical Engineering, Xiamen University, Xiamen 361005, PR. China.
E-mail addresses: wangmengheng@xmu.edu.cn (M. Wang), kangcheng@xmu.edu.cn (K. Cheng), zhangqh@xmu.edu.cn (Q. Zhang).
[1] These authors contributed equally.

efficiency of green H_2.

With the feeding of H_2, CO_2 can be hydrogenated to a variety of hydrocarbon products, including methanol [25,26], dimethyl ether [27], lower olefins [28], higher alcohols [29], and liquid fuels [30]. In 2016, Bao's and our group reported a series of metal(oxide)-zeolite catalysts for the direct and selective synthesis of lower olefins from syngas (H_2/CO) [31,32]. Since then, bifunctional catalysis has been widely applied in the direct transformation of C1 molecules, especially CO_2, into hydrocarbon products with ultrahigh selectivities [33–35]. These bifunctional routes can be roughly categorized into two types, i.e. the methanol-mediated route by the oxide-zeolite catalyst and the modified Fischer-Tropsch (FT) synthesis route by the iron-zeolite catalyst [21,33,36]. The oxide-zeolite catalyst allows the direct synthesis of lower olefins, aromatics, and gasoline hydrocarbons with ultrahigh selectivities, but is accompanied by low activity and high CO selectivity. While iron-zeolite catalyst can offer higher activity and low CO selectivity, but relatively wide product distribution, rendering it suitable for the production of hydrocarbon fuels [37,38].

Wei et. al. reported the direct hydrogenation of CO_2 into gasoline (C_5-C_{11}) hydrocarbons with a selectivity of 78% at CO_2 conversion of 22% over a Na-Fe_3O_4/H-ZSM-5 multifunctional catalyst at 320 °C [39]. By the combination of the sodium-modified spinel oxide $ZnFeO_x$ and hierarchical nanocrystalline H-ZSM-5 aggregates, Gao et al. further increased the CO_2 conversion to 41% and improved the content of aromatics in hydrocarbon products [40]. Generally, the product distribution of bifunctional catalysts is controlled by zeolite function and H-ZSM-5 with ten-membered-ring (10MR) openings exhibited the highest selectivity towards liquid fuels and aromatics [41–45]. While, the modification of iron catalysts can regulate the RWGS and FT synthesis performances, thus leading to adjustable CO_2 conversion, CO selectivity, and olefin contents in hydrocarbon products [46–48]. Besides, in this bifunctional or multifunctional system, the integration manners, which determines the proximity between different functional sites, also impacted the synergy of metal-acid catalysis and catalyst stability [49–51]. The harsh reaction conditions, including high temperature, reductive atmosphere, and the formation of water vapor, often induce a dramatic change in catalyst properties during the reaction [52].

Thus, many research efforts have been devoted to optimizing catalyst composition for better compatibility and proximity control for better stability [39,41]. Despite these promising results from the catalyst aspect, further improvements in catalytic performance, and an in-depth understanding of catalyst deactivation and reaction network under harsh reaction conditions are still indispensable before the successful implementation of CO_2 upcycling.

In this work, we have assessed the performance of upcycling CO_2 into hydrocarbon fuels and chemicals by coupling with green H_2 under industrially preferred high temperatures up to 400 °C. The bifunctional iron-zeolite catalysts have been intensively optimized from the aspects of metal promotion (e.g. alkali metals, alkaline-earth metals, and transition metals), zeolite topologies with a particular focus on micropore sizes (8MR, 10MR and 12MR openings), and integration manners. The optimized FeMnK+ZSM-5 could provide a C_5-C_{11} hydrocarbon selectivity of 70% at CO_2 conversion of 27% with a stability of 100 h at 320 °C. The side product was mainly C_2-C_4 olefins with a selectivity of 17%. The CO_2 conversion levels and the yield of hydrocarbon fuels could be further enhanced with temperatures raised to 400 °C, and CO selectivity was as low as around 15%, showing excellent high-temperature application potential. Moreover, the key factors determining the catalytic performances, dynamic evolution of active sites, and reaction network have been intensively investigated and clarified.

2. Experimental

2.1. Materials

Iron nitrate ($Fe(NO_3)_3 \cdot 9 H_2O$), manganese nitrate (Mn ($NO_3)_2 \cdot 4 H_2O$), potassium nitrate (KNO_3), and citric acid were purchased from Sinopharm Chemical Reagent. Pseudoboehmite (Al_2O_3, 72 wt%), orthophosphoric acid (H_3PO_4, 85 wt%), hydrofluoric acid (HF, 40 wt%), and dichloromethane (CH_2Cl_2) were purchased from Beijing Reagents Company. Aluminum isopropanol (98%), silica solution (30 wt %), triethylamine (TEA, 99%), and di-*n*-propylamine (DPA, 99%) were purchased from Sigma-Aldrich. H-SSZ-13, H-MOR, H-Beta, and H-Y were purchased from Shanghai Saint Chemical Materials Co. Ltd. H-
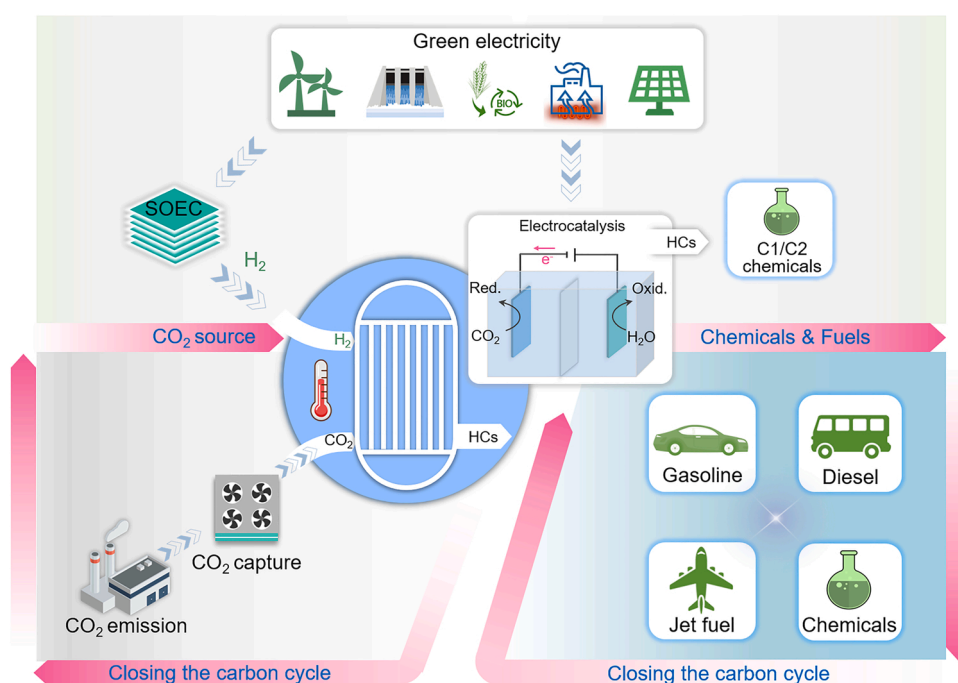

Fig. 1. Flowsheet diagram for integrating CO_2 conversion with the SOEC system to construct a carbon neutralization network. In future energy systems, significant synergies can be obtained by utilizing green H_2 to convert CO_2 into various target products (e.g., gasoline, diesel, jet fuel, and high-value chemicals such as olefins and aromatics).

ZSM-35, H-MCM-22, and H-ZSM-22 were purchased from Nanjing Xianfeng Nano Material Technology Co. Ltd. H-ZSM-5 and H-ZSM-48 zeolites with different atomic ratio of Si/Al were purchased from Nankai University Catalyst Co. Ltd.

2.2. Catalyst synthesis

Fe*M* oxides were synthesized by a sol-gel method with a Fe/*M* atomic ratio of 40/1 (at/at) (*M* = Li, Na, K, Rb, Cs, Ca, Co, Al, Mg, Cu, Zn, and Mn). Pure Fe_2O_3 oxide was obtained without second metal. Specifically, for FeK oxides, 10 g of $Fe(NO_3)_3 \cdot 9 H_2O$, 0.063 g of KNO_3, and 12 g of citric acid were dissolved into 30 mL of deionized water. The mixture was evaporated at 90 °C by stirring until a viscous gel was obtained, after which the gel mixture was heated to 180 °C for 3 h and calcined at 500 °C in the air for 5 h. By adjusting the amount of KNO_3, FeK oxides with different atomic ratios of Fe/K could be synthesized by the same method. After replacing KNO_3 with other metal nitrates, a series of different Fe*M* oxides were prepared. For FeK (40/*x*) and FeMn (40/*y*) (*x*, *y* = 0, 1, 4) oxides, 40/*x* and 40/*y* represented the atomic ratio of Fe/K and Fe/Mn, respectively. In this work, Fe*M* was the abbreviation for the Fe-based oxides with a Fe/*M* ratio of 40:1 (at/at) (*M* = Li, Na, K, Rb, Cs, Ca, Co, Al, Mg, Cu, Zn, and Mn) unless otherwise mentioned.

FeMnK oxides were also synthesized by the sol-gel method as mentioned for the synthesis of the Fe*M* catalyst above. The atomic ratio of Fe/Mn over FeMnK oxides was fixed at 40/4. The obtained catalysts were named FeMnK (40/4/*z*) (*z* = 0, 1, 4, 16) oxides. 40/4/*Z* represents the atomic ratio of Fe/Mn/K. In this work, FeMnK was the abbreviation for the FeMnK oxides with a Fe/Mn/K ratio of 40/4/4 unless otherwise mentioned. SAPO-34, SAPO-11, and SAPO-5 zeolites were synthesized according to our previous work [53].

H-ZSM-5 zeolite with a mesostructure was prepared by alkaline treatment [54]. Typically, 10 g of parent H-ZSM-5 with an atomic Si/Al ratio of 27 were added into 100 mL NaOH aqueous solutions with a concentration of 0.6 M. Then, the suspension was heated to 80 °C and stirred continuously for 2 h. After cooling to room temperature, the solid product was recovered by filtration, washed with deionized water three times, and dried at 100 °C for 6 h. Subsequently, the NH_4^+ exchange was performed using an NH_4Cl aqueous solution. After the exchange, the solid product was collected by filtration followed by washing, drying, and calcination at 550 °C for 6 h. The above exchange process was repeated three times, and the obtained sample was denoted as *meso*-H-ZSM-5.

The mass ratio of Fe-based oxide and zeolite in this work was fixed at 1:1. The Fe-based oxide and zeolite powders were pressed, crushed, and sieved to granules of 30–60 meshes (sizes, 250–600 μm) for use, respectively. The bifunctional catalysts composed of FeMnK oxide and zeolites with other topology structures, except H-ZSM-5, were only prepared by a granule-mixing method, denoted as FeMnK+zeolite. The bifunctional catalysts composed of FeMnK and H-ZSM-5 were specially prepared by three different integration manners. They were denoted as (i) FeMnK‖H-ZSM-5: The dual-bed with FeMnK oxide granules (250–600 μm) in the upstream bed and H-ZSM-5 granules (250–600 μm) in the downstream bed, separated by quartz wool with 3 mm thickness. (ii) FeMnK+H-ZSM-5: The stacking of FeMnK and H-ZSM-5 zeolite individual with 30–60 meshes (250–600 μm). (iii) FeMnK/H-ZSM-5: The fine FeMnK and H-ZSM-5 zeolite powders were physically mixed in a mortar for 10 min, then pressed, crushed, and sieved to granules of 30–60 meshes.

2.3. Catalyst characterization

X-ray powder diffraction (XRD) measurements were performed on a Rigaku Ultima IV diffractometer. The Cu Kα radiation (λ = 0.15406 nm) generated at 40 kV and 30 mA was used as the X-ray source. N_2-physisorption measurements were performed on a Micromeritics Tri-Star II 3020 Surface Area Analyzer. Before N_2 adsorption, the sample was first degassed under a vacuum at 200 °C for 2 h. X-ray fluorescence (XRF) spectroscopy, which could provide information of Si/Al and Si/(Si+Al+P) ratio of the zeolites, was analyzed with an S8 TIGER XRF instrument with rhodium target (50 kV, 50 mA). Scanning electron microscopy (SEM) measurements were performed on a Hitachi S-4800 operated at 15 kV. Transmission electron microscopy (TEM) measurements were carried out on a Phillips Analytical FEI Tecnai20 electron microscope operated at an acceleration voltage of 200 kV. Pyridine-adsorption FTIR (Py-FTIR) profiles were performed on the Nicolet 6700 instrument equipped with an MCT detector. After being pretreated under vacuum at 400 °C for 2 h, the sample was cooled to 150 °C. Then pyridine vapor was introduced slowly into the sample cell at 150 °C for 10 min. FT-IR spectra were recorded after gaseous or weakly adsorbed pyridine molecules were removed by evacuation at 150 °C. H_2 temperature-programmed reduction (H_2-TPR) measurements were conducted on a Micromeritics AutoChem II 2920 instrument. Typically, 100 mg of the samples were firstly pre-treated by high-purity helium at 400 °C and then heated from 50 °C to 800 °C in the 5% H_2-Argon (5 vol% H_2) atmosphere. CO_2 temperature-programmed desorption (CO_2-TPD) measurements were performed on the Micromeritics AutoChem II 2920 instrument. Typically, 100 mg of the samples were firstly reduced with high-purity hydrogen flow at 400 °C. After then, the adsorption of CO_2 was performed at 50 °C in the 10% CO_2-argon (10 vol% CO_2) atmosphere, and the TPD was measured in the He gas flow by raising the temperature from 50 °C to 600 °C. NH_3 temperature-programmed desorption (NH_3-TPD) measurements were also performed on a Micromeritics AutoChemII 2920 instrument. Typically, 100 mg of the sample was pre-treated in a quartz reactor with a purge of high-purity helium. The NH_3 adsorption was performed at 100 °C in an NH_3-He mixture (10 vol% NH_3) for 1 h, followed by TPD in He flow by raising the temperature to 600 °C at a ramp rate of 10 °C min^{-1}. The content of formed coking species in the reacted catalysts was measured by thermal gravimetric (TG) analysis on a TGA Q500 instrument. The temperature was first raised to 100 °C for 2 h to remove physically adsorbed water, followed by raising the temperature to 800 °C under airflow. The carbonaceous compounds retained in the reacted catalysts were analyzed by GC-MS (Agilent 7890 A/5975 C) with a capillary column of HP-5, an FID detector, and a mass-sensitive detector. An HF solution (40 wt%) was used to dissolute the reacted catalysts, after which the carbonaceous compounds were extracted using CH_2Cl_2.

2.4. Catalyst evaluation

The CO_2 conversion was performed on a high-pressure fixed-bed reactor built by Xiamen HanDe Engineering Co., Ltd. Typically, 0.15 g of Fe-based oxide or 0.3 g of the bifunctional catalyst with grain sizes of 250–600 μm (30–60 meshes) was loaded in a titanium reactor (inner diameter, 10 mm). Before the reaction, the catalyst was pre-treated in the reactor with an H_2 flow (30 mL min^{-1}) at 400 °C for 2 h and then cooled to room temperature. After that feed gas with an H_2/CO_2 molar ratio of 3:1 and a pressure of 3.0 MPa was introduced into the reactor. Argon with a concentration of 4.0 vol% in the feed gas was used as an internal standard for calculating the CO_2 conversion. The temperature was raised to 320 or 400 °C at a rate of 2 °C min^{-1} to start the reaction.

Products were analyzed by online gas chromatography equipped with a thermal conductivity detector (TCD) and two flame ionization detectors (FID). A TDX-01 packed column was connected to TCD, while RT-Q-BOND-PLOT and HP-PONA capillary columns were connected to FID. The CO_2 conversion and the product selectivity were calculated on a carbon basis. Carbon balances were all higher than 95%. Except for special instructions, the catalytic activity and product selectivity in the present study were obtained at around time on stream (TOS) of 5 h.

3. Results and discussion

3.1. Effect of metal promoters

We first investigated the effect of metal promoters on catalytic behaviors of Fe*M* catalysts for CO_2 hydrogenation (Fig. 2a). The pure Fe_2O_3 catalyst exhibited a CO_2 conversion of 33% with a CO selectivity of 14% at 320 °C (Table S1). CO_2 conversion and CO selectivity of Fe*M* catalysts were similar to those of the pure Fe_2O_3 catalyst, but the product distribution depended on the varieties of metal promoters (Fig. 2a). The product over the pure Fe_2O_3 catalyst was mainly saturated paraffins, including 46% of CH_4 and 35% of C_2–C_4 paraffins (C_2–C_4^0). With the addition of a small amount of K (Fe/K = 40/1, atomic ratio), the selectivity of both C_2–C_4 olefins (C_2–$C_4^=$) and C_{5+} hydrocarbons increased remarkably to 36% and 46%, respectively, whereas the selectivity of CH_4 and C_2–C_4^0 decreased dramatically to 12% and 5.9%, respectively (Fig. 2a and Table S1). Compared with Fe_2O_3 with a chain growth factor (α) of 0.47, the α value increased to 0.62 over FeK (Table S1). The promotion effect of monovalent alkali metals on the formation of C_2–$C_4^=$ and C_{5+} hydrocarbons over Fe-based catalysts was also observed at 400 °C (Fig. 2b and Table S2). Further increasing the K content did not affect the catalytic performance (Fig. 2c), indicating that a small amount of K was sufficient to modify iron catalysts. Although the selectivity of C_2–$C_4^=$ over FeRb slightly decreased to 21%, it is still much higher than 7.0% over Fe_2O_3 (Fig. 2b).

Relatively, divalent or trivalent metal promoters exhibited a minor impact on the product distribution and the α values compared to pristine Fe_2O_3, except Mn (Fig. 2a–b and Table S1). CO selectivity over FeMn oxides could be further decreased with the increase of Mn content,

without compromise in CO_2 conversion (Fig. 2c). Through co-modification by K and Mn, the selectivity of C_5–C_{11} and C_2–$C_4^=$ over FeMnK could reach up to 45% and 36% respectively at 320 °C (Fig. 2c). It is noteworthy that the selectivity of high-value C_{2+} olefins over FeMnK (40/4/4) could reach 73% (Table S3). As the reaction temperature was raised to 400 °C, the promotion in the formation of olefins and C_5–C_{11} hydrocarbons was still observed (Table S4) and this characteristic offers the potential for bifunctional FeMnK+zeolite catalysts to tune the product distribution by oligomerization, isomerization, and aromatization.

To reveal the effects of metal promotes on the iron structure, the Fe*M* catalysts were subjected to XRD studies (Fig. 3a and Fig. S1). The diffraction peaks attributed to the α-Fe_2O_3 phase were observed in both Fe_2O_3 and Fe*M* (40/1). The addition of monovalent alkali metals could lead to the formation of Fe_3O_4 together with α-Fe_2O_3 (Fig. S1a), while the addition of divalent or trivalent metals did not affect the crystal structure of α-Fe_2O_3 (Fig. S1b). As the atomic ratio of Fe/Mn increased from 40/1 to 40/4, the crystal structure remained α-Fe_2O_3 (Fig. S2). No diffraction peak relevant to the MnO_x phase was found, indicating the formation of a solid solution of hematite (α-$(Fe_{1-x}Mn_x)_2O_3$) [55]. As the atomic ratio of Fe/K increased from 40/1–40/4, the crystal structure became Fe_3O_4 at the expense of α-Fe_2O_3, resulting from the electron donation of alkali metals for the stabilization of Fe_3O_4 [56]. By analyzing the iron phases semi-quantitatively by XRD, it was found that the addition of K rather than Mn could regulate the composition of the Fe phase (Fig. 3b). By the TEM and SEM imaging of Fe*M* (40/1) oxides, the addition of monovalent alkali metals could more obviously reduce the particle size of iron oxide than that of divalent or trivalent metals (Fig. S3–S5). The BET surface area of FeMn (18 $m^2 g^{-1}$) was close to that
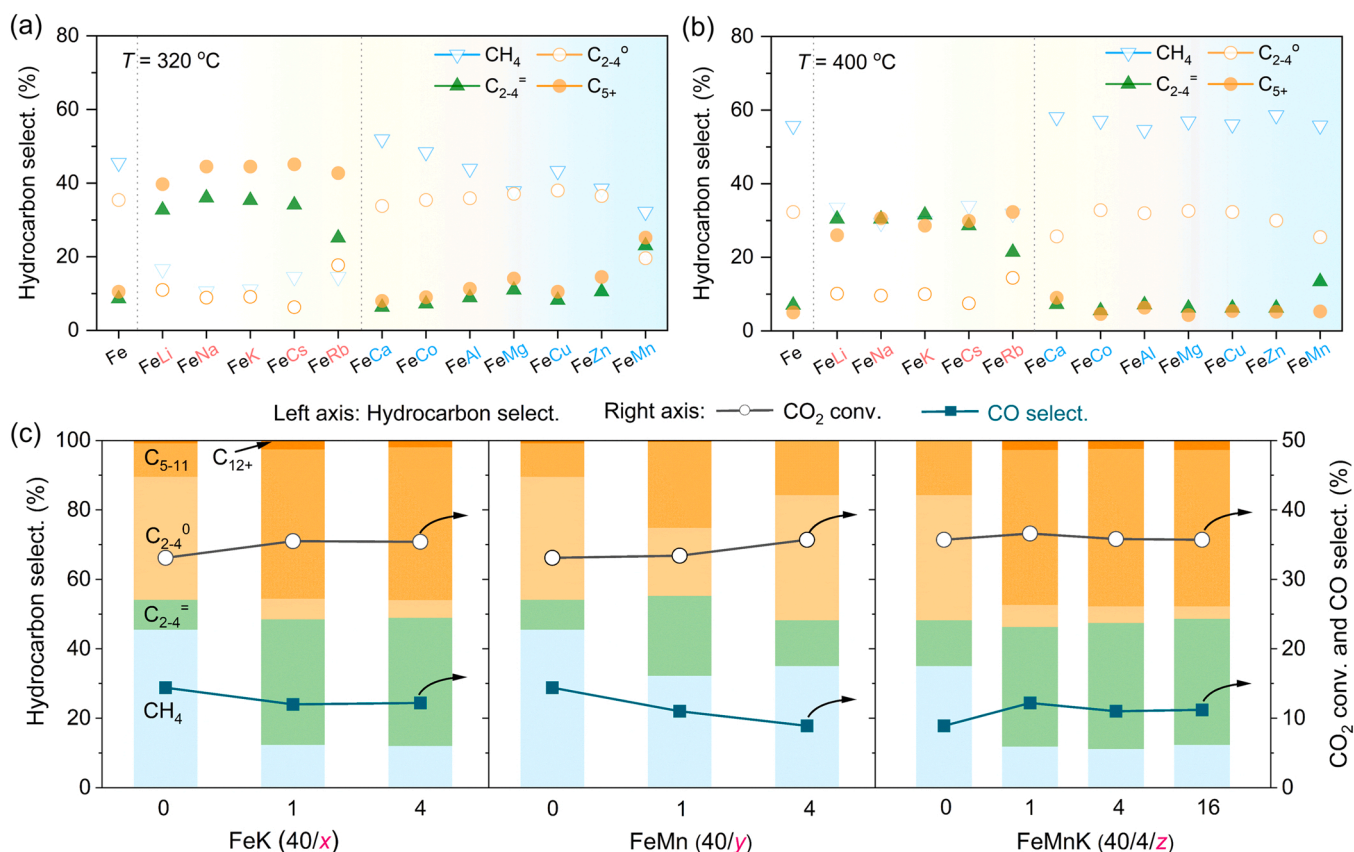

Fig. 2. Effect of (a−b) metal promoters, (c) K content and Mn content of Fe-based oxides on the hydrocarbon selectivity in CO_2 hydrogenation. Reaction conditions: T = 320 or 400 °C; P = 3 MPa; H_2/CO_2 = 3:1; F = 15 mL min^{-1}; $m_{cat.}$ = 0.15 g; Time on stream = 5 h. (a) Fe*M* (40/1), 320 °C; (b) Fe*M* (40/1), 400 °C; (c) FeK (40/*x*) oxides, FeMn (40/*y*) and FeMnK (40/4/*z*) oxides, 320 °C. *M* represents the different metal promoters. The atomic ratio of Fe/*M* was fixed at 40/1 in Fig. 2a–b. 40/*x*, 40/*y*, and 40/4/*z* represent the atomic ratio of Fe/K, Fe/Mn, and Fe/Mn/K in Fig. 2c, respectively. Details for catalytic performance and reaction conditions can be found in Tables S1–S3.
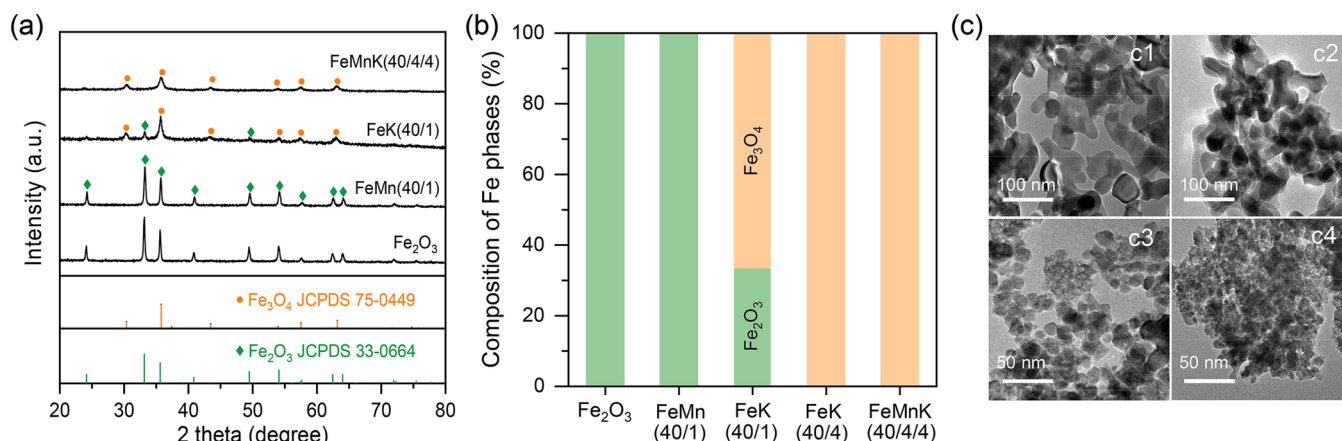
Fig. 3. (a) XRD patterns, (b) the composition of Fe phases, and (c) TEM images of (c1) Fe_2O_3, (c2) FeMn (40/1), (c3) FeK (40/1), and (c4) FeMnK (40/4/4) oxides, respectively. The composition of Fe_2O_3 and Fe_3O_4 in Fig. 3b was semi-quantitative according to the peak intensity of 33.2° and 35.7° in Fig. S2.

of Fe_2O_3 (17 $m^2 g^{-1}$), while the BET surface area of FeK (54 $m^2 g^{-1}$) was twice larger (Table S5). With the co-promotion of K and Mn, the particle size of the oxides reduced from 50 nm to 10 nm (Fig. 3c), and the BET surface area increased from 17 $m^2 g^{-1}$ to 68 $m^2 g^{-1}$ (Table S5). The above characterization results suggest that the addition of monovalent alkali metals could effectively decorate the electron state of iron and promote the dispersion of iron catalysts, resulting in the outstanding performance of FeMnK oxides in CO_2 hydrogenation.

3.2. Zeolite properties

Acidic zeolite plays a key role in reaction pathways and steers product distribution [57]. For clarity, the zeolites were classified according to their characteristic pore size, including (i) H-SSZ-13 (CHA) with 8MR micropores, (ii) H-ZSM-35 (FER), H-MCM-22 (MWW), H-ZSM-22 (TON), H-ZSM-5 (MFI) and H-ZSM-48 (MRE) zeolites with 10MR micropores, and (iii) H-MOR (MOR), H-Beta (BEA) and H-Y (FAU) zeolites with 12MR micropores.

The primary characteristics of these nine zeolites with different topology structures were carefully investigated and summarized (Table S6 and S7). Compared with the corresponding JCPDS cards, XRD patterns of these zeolites confirm their matched structures and high crystallinity nature (Fig. S6a–i). The Al content of these zeolites and the density of strong acid sites were measured by XRF and NH_3-TPD experiments, respectively. The strong acid sites of zeolites could be generally regarded as the Brönsted acid sites (BAS), relating to the replacement of Si with Al atom in the zeolite framework [58,59]. Despite the difference in the zeolite topology, the densities of strong acid sites became higher with the increase of Al content (Table S8).

The SEM imaging suggests that H-ZSM-48 and H-MOR were composed of large single crystals with sizes larger than 1 μm, and other zeolites exhibited nano-scale sizes (Fig. S7a–i). H-SSZ-13, H-ZSM-35, H-ZSM-5, and H-Y zeolites displayed cube, sheet, cuboid, and octahedron morphology, respectively, with particle sizes in the range of 300 − 600 nm, and these were the typical morphology of CHA, FER, MFI and FAU structures [60–63]. H-MCM-22, H-ZSM-22, and H-Beta zeolites displayed regular shapes composed of nanorods or nanospheres with particle sizes in the range of 100 − 700 nm. The varieties in the morphology of these zeolites relied on their intrinsic difference with topology structures and the different organic templates used in hydrothermal synthesis [64]. Nevertheless, the surface area and morphology of these zeolites were similar to those published elsewhere (Table S6) [62,65,66]. It is commonly accepted that product distribution of CO_2 hydrogenation mainly relies on the topology structures of zeolites [41], while the crystal morphology might affect catalytic stability [67,68]. These insights allow us to deeply investigate the effects of topology

structures on the product distribution in CO_2 hydrogenation.

3.3. Overview of the zeolite topology effect

The pre-optimized FeMnK was then integrated with zeolites with different topologies by the granule-mixing method and was evaluated for CO_2 hydrogenation at 320 °C (Fig. 4 and Table S9). Generally, the CO_2 conversion and CH_4 selectivity were in the similar range of 30–36% and 10–12%, respectively, independent of zeolite topology. The CO selectivity was below 24% for all catalysts, significantly lower than the emerging bifunctional oxide/H-ZSM-5 catalysts [17,30,41]. Compared with FeMnK (Fig. 2c), the integration with H-SSZ-13 with small 8MR micropores had no obvious effect on the product selectivity (Fig. 4a and Table S9). The combination of H-ZSM-35 with both 8MR and 10MR micropores decreased the selectivity of C_2–$C_4^=$ and C_5–C_{11} hydrocarbons (Fig. 4b and Table S9). Therefore, H-SSZ-13 and H-ZSM-35 were not suitable for catalyzing the formation of C_5–C_{11} hydrocarbons. Notably, with the pore size increasing to only 10MR, the selectivity of C_5–C_{11} hydrocarbons exceeded 50% over FeMnK+H-MCM-22, FeMnK+H-ZSM-22, FeMnK+H-ZSM-5 and FeMnK+H-ZSM-48 catalysts, in the sequence of H-ZSM-5 (61%) > H-ZSM-22 (54%) > H-MCM-22 (50%) = H-ZSM-48 (50%) (Fig. 4c–f and Table S9). When the H_2/CO_2 ratio was reduced from 3.0 to 2.0, a 70% selectivity of C_5–C_{11} hydrocarbons together with a 17% selectivity of C_2–$C_4^=$ was obtained over FeMnK+H-ZSM-5 catalyst (Table S10). In addition, the introduction of mesopores into the microporous zeolite can also improve the selectivity of C_5–C_{11} to 70% at the H_2/CO_2 ratio of 3.0 (Table S11 and S12). It is noteworthy that the FeMnK+H-ZSM-5 catalyst deactivated faster at $H_2/CO_2 = 2$ than at $H_2/CO_2 = 3$ (Fig. S8), probably because of the formation of heavy aromatic hydrocarbons at low H_2 partial pressure. The selectivity of C_2–$C_4^=$, which was the precursor for oligomerization and aromatization, was significantly lower on the 10 MR zeolites compared to FeMnK. FT synthesis only produces linear hydrocarbons, but the proportion of aromatics in the C_5–C_{11} hydrocarbons over FeMnK+H-ZSM-5 reached up to 42% (Table S13), owing to the matched pore sizes and channel bending of ZSM-5 with aromatics [69,70]. H-MOR, H-Beta, and H-Y zeolites with large 12MR micropores were also employed for building bifunctional catalysts, and it was found that the selectivity of C_5–C_{11} was lower than FeMnK, even less than 40% (Fig. 4g–i and Table S9).

In addition, by adjusting the density of BAS over H-ZSM-5 and ZSM-48 zeolites, the selectivity of C_5–C_{11} hydrocarbons remained at about 63% and 50%, respectively (Table S13). As long as a certain density of BAS existed, the total selectivity of C_5–C_{11} hydrocarbons was not sensitive to zeolite acidity, but the olefin/paraffin ratio of C_2–C_4 decreased significantly with the increase in BAS density (Table S13). Besides,
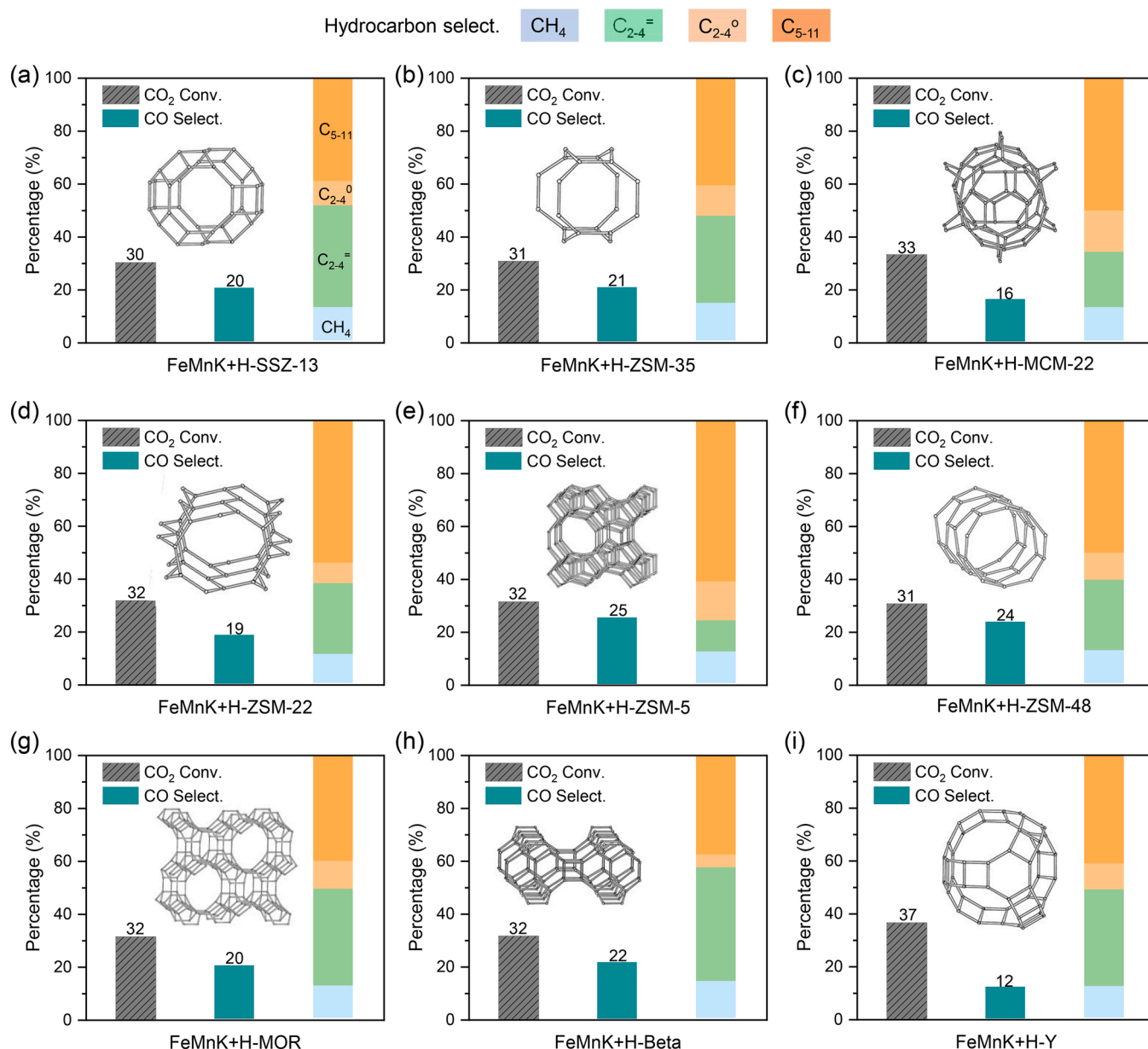
Fig. 4. Effect of framework topology of zeolites on the catalytic performances at 320 °C of FeMnK+zeolite catalysts in CO_2 hydrogenation. (a) FeMnK+H-SSZ-13, (b) FeMnK+H-ZSM-35, (c) FeMnK+H-MCM-22, (d) FeMnK+H-ZSM-22, (e) FeMnK+H-ZSM-5, (f) FeMnK+H-ZSM-48, (g) FeMnK+H-MOR, (h) FeMnK+H-Beta and (i) FeMnK+H-Y. Reaction conditions: Catalyst, FeMnK+zeolite (1/1), Granule-mixing; T = 320 °C; P = 3 MPa; H_2/CO_2 = 3:1; F = 30 mL min^{-1}; $m_{cat.}$ = 0.30 g; Time on stream = 5 h. Details for catalytic performance and reaction conditions can be found in Table S9.

FeMnK+SAPO-34, FeMnK+SAPO-11, and FeMnK+SAPO-5 catalysts with weak acid sites were also investigated in CO_2 hydrogenation (Table S9). It was found that the selectivities of C_2–C_4 and C_5–C_{11} hydrocarbons almost remained at about 42% and 45% over all the FeMnK+SAPO catalysts, i.e. no promotion effect was observed over SAPO-based catalysts. Overall for Si-Al zeolites, the product distribution of FeMnK/zeolite was strongly governed by the topology structure of zeolites, and the influence of zeolite acidity played a secondary role on the catalytic performances in CO_2 hydrogenation.

3.4. Reaction at 400 °C

To efficiently utilize the H_2 from SOEC and CO_2 from combustion, bifunctional catalysts sometimes have to operate under high reaction temperatures. The reaction temperature is considered an important factor, influencing CO_2 conversion, CO selectivity, and hydrocarbon selectivity, especially for the distribution of C_5–C_{11} hydrocarbons [71]. However, the CO_2 hydrogenation reaction over bifunctional iron-zeolite tandem catalysts was often performed at below 350 °C [39,40,72]. To evaluate the catalytic behavior at higher temperatures, we carefully investigated FeMnK+H-MCM-22, FeMnK+H-ZSM-22, FeMnK+H-ZSM-5, and FeMnK+H-ZSM-48 catalysts in CO_2 hydrogenation at 400 °C (Fig. 5a–d and Table S14).

As the temperature increased from 320 °C to 400 °C, CO_2 conversion improved from about 30–50% over FeMnK+H-MCM-22, FeMnK+H-ZSM-22, FeMnK+H-ZSM-5, and FeMnK+H-ZSM-48 catalysts (Table S14). The selectivity of C_5–C_{11} hydrocarbons reduced while the selectivity of CH_4 increased significantly. The selectivity changes of C_2–$C_4^=$ and C_2–C_4^0 were not regular due to the different acid densities of these zeolites. However, the total selectivity of C_2–$C_4^=$ and C_2–C_4^0 was relatively stable in the range of 31–38% over the catalysts evaluated at either 320 °C or 400 °C (Table S9 and S14). The selectivity of C_5–C_{11}
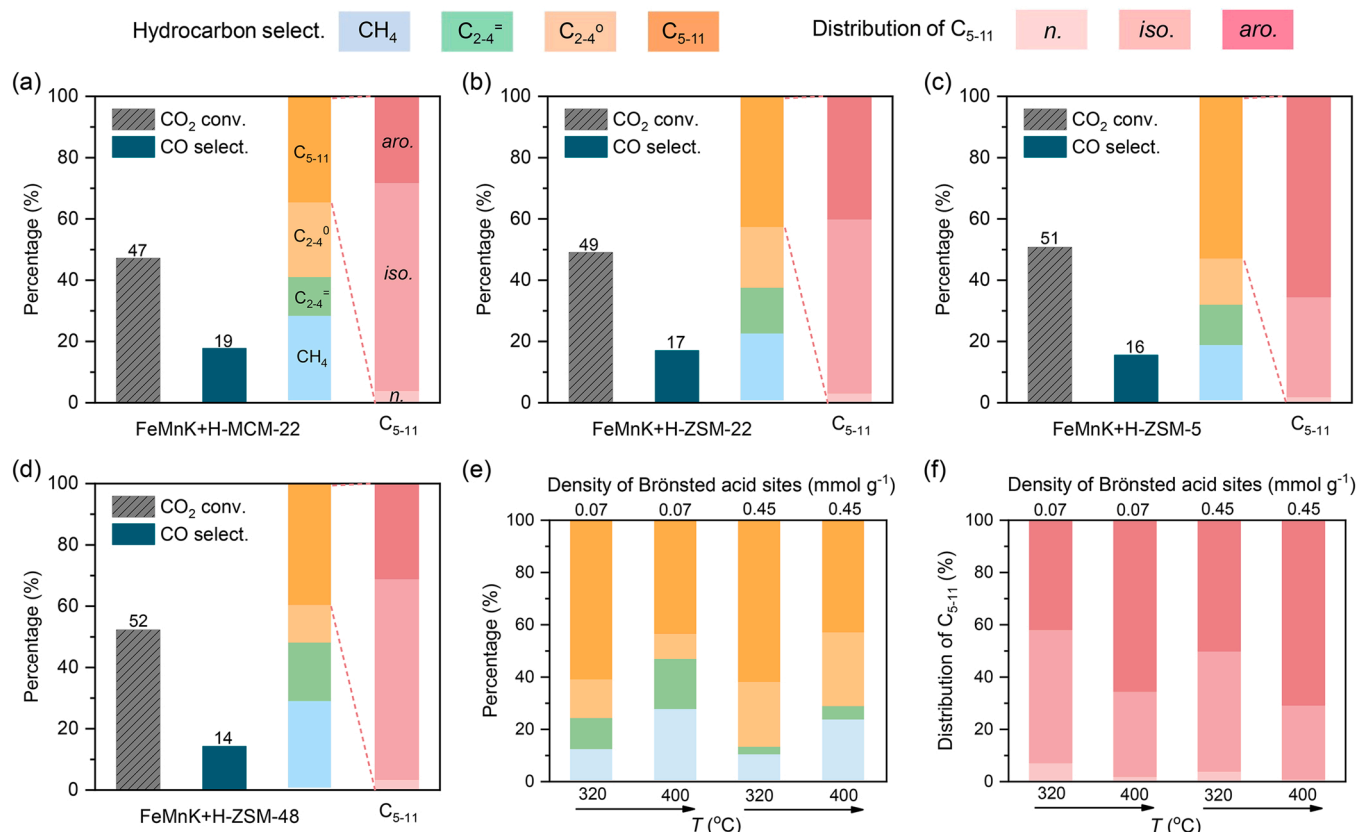
Fig. 5. (a–d) Effect of framework topology of 10MR zeolites on the catalytic performances at 400 °C of FeMnK+zeolite catalysts in CO_2 hydrogenation. (a) FeMnK+H-MCM-22, (b) FeMnK+H-ZSM-22, (c) FeMnK+H-ZSM-5, (d) FeMnK+H-ZSM-48. (e–f) Effect of temperature and the densities of BAS of H-ZSM-5 on (e) the hydrocarbon selectivity and (f) the distribution of C_{5-11} of FeMnK/zeolite catalysts in CO_2 hydrogenation. Details for catalytic performance and reaction conditions can be found in Tables S14–S15.

hydrocarbons over FeMnK+H-ZSM-5 remained at 53% at 400 °C, only 8% lower than that at 320 °C. Therefore, H-ZSM-5 is suitable for producing C_5–C_{11} hydrocarbons in a wide range of temperatures.

The thermodynamic analysis clarified that RWGS (CO_2 + H_2 = CO+H_2O) is promoted at higher temperatures (Fig. S9a). However, CO selectivity did not increase significantly as the reaction temperature over our bifunctional catalysts, and even CO selectivity decreased from 25% to 16% over the FeMnK+H-ZSM-5 catalyst (Table S14). This indicated the high FT activity of the iron catalysts at 400 °C, suppressing the CO selectivity. Based on the thermodynamic analysis, the formation of benzene was slightly more favorable than n-hexane and 2-methyl pentane in CO_2 hydrogenation at 400 °C (Fig. S9a). Besides, the equilibrium conversion levels of CO_2 hydrogenation to benzene, n-hexane, and 2-methyl pentane are higher than 70% (Fig. S9b), indicating the CO_2 conversion (~ 50%) at 400 °C was not limited by the thermodynamics (Fig. 5).

Comparing the distribution of C_5–C_{11} hydrocarbons over bifunctional catalysts, the proportion of aromatics increased with reaction temperature despite the slight decrease in C_5–C_{11} selectivity (Fig. 5e–f). Over bifunctional catalysts with BAS density of 0.07 mmol g^{-1}, the proportion of aromatics increased from 42% to 65% from 320 °C to 400 °C in the C_5–C_{11} range. By optimizing the BAS density of H-ZSM-5, the proportion of aromatics could reach 71% at 400 °C (Table S15). The formation of C_5–C_{11} isomers was dominant over FeMnK+H-MCM-22, FeMnK+H-ZSM-22, and FeMnK+H-ZSM-48 catalysts. The proportion of isomers over FeMnK+H-MCM-22 could reach 68% at 400 °C, mainly because H-MCM-22 possesses a unique lamellar structure consisting of two independent and nonintersecting pore systems, matching well the C_5–C_{11} *iso*-paraffins [62]. From 320 °C to 400 °C, the yield of aromatics increased more than doubled over almost all the bifunctional catalysts

(Table S16). Among these bifunctional catalysts, FeMnK+H-ZSM-5 was the most effective to catalyze the formation of aromatics at 400 °C.

3.5. Effect of pore size

The dependence of C_5–C_{11} and C_2–$C_4^=$ selectivity of FeMnK+zeolite catalysts on the pore size of zeolites in CO_2 hydrogenation was summarized, respectively (Fig. 6a and S10). Overall, a volcano trend was observed between the selectivity of C_5–C_{11} hydrocarbons and the pore sizes, while an opposite trend was shown between the selectivity of C_2–$C_4^=$ and the pore sizes of Si-Al zeolites. The selectivities of C_2–$C_4^=$ and C_5–C_{11} hydrocarbons were 36% and 45% over FeMnK, respectively (Fig. 2c). The selectivity of C_5–C_{11} hydrocarbons reduced while that of both C_2–$C_4^=$ and C_2–C_4^0 increased slightly over FeMnK+H-SSZ-13 (0.38 ×0.38 nm²) catalyst (Table S9). H-ZSM-35 (0.42 ×0.55 nm²) zeolite has both the 10MR and 8MR pores, but the selectivity of C_5–C_{11} hydrocarbons was still poor (Table S9). H-MCM-22 (0.40 ×0.55 nm²), H-ZSM-22 (0.46 ×0.57 nm²), H-ZSM-5 (0.53 ×0.56 nm²), and H-ZSM-48 (0.56 ×0.56 nm²) zeolites only have 10MR pores. The selectivity of C_5–C_{11} hydrocarbons over FeMnK+H-MCM-22, FeMnK+H-ZSM-22, FeMnK+H-ZSM-5, and FeMnK+H-ZSM-48 catalysts were more than 50% (Fig. 6a), higher than that maximum value that ASF model predicted. Correspondingly, the selectivity of C_2–$C_4^=$ was lower than that of FeMnK (Fig. S10). One may expect the product distribution could shift to heavier hydrocarbons over H-MOR (0.65 ×0.70 nm²), H-Beta (0.66 ×0.77 nm²), and H-Y (0.74 ×0.74 nm²) zeolites with large 12MR pores. However, the formation of C_5–C_{11} was inhibited over the three zeolites in CO_2 hydrogenation (Fig. 6a).

To investigate the formation mechanism of C_5–C_{11} hydrocarbons over the FeMnK+zeolites catalysts, the product over FeMnK, FeMnK+H-
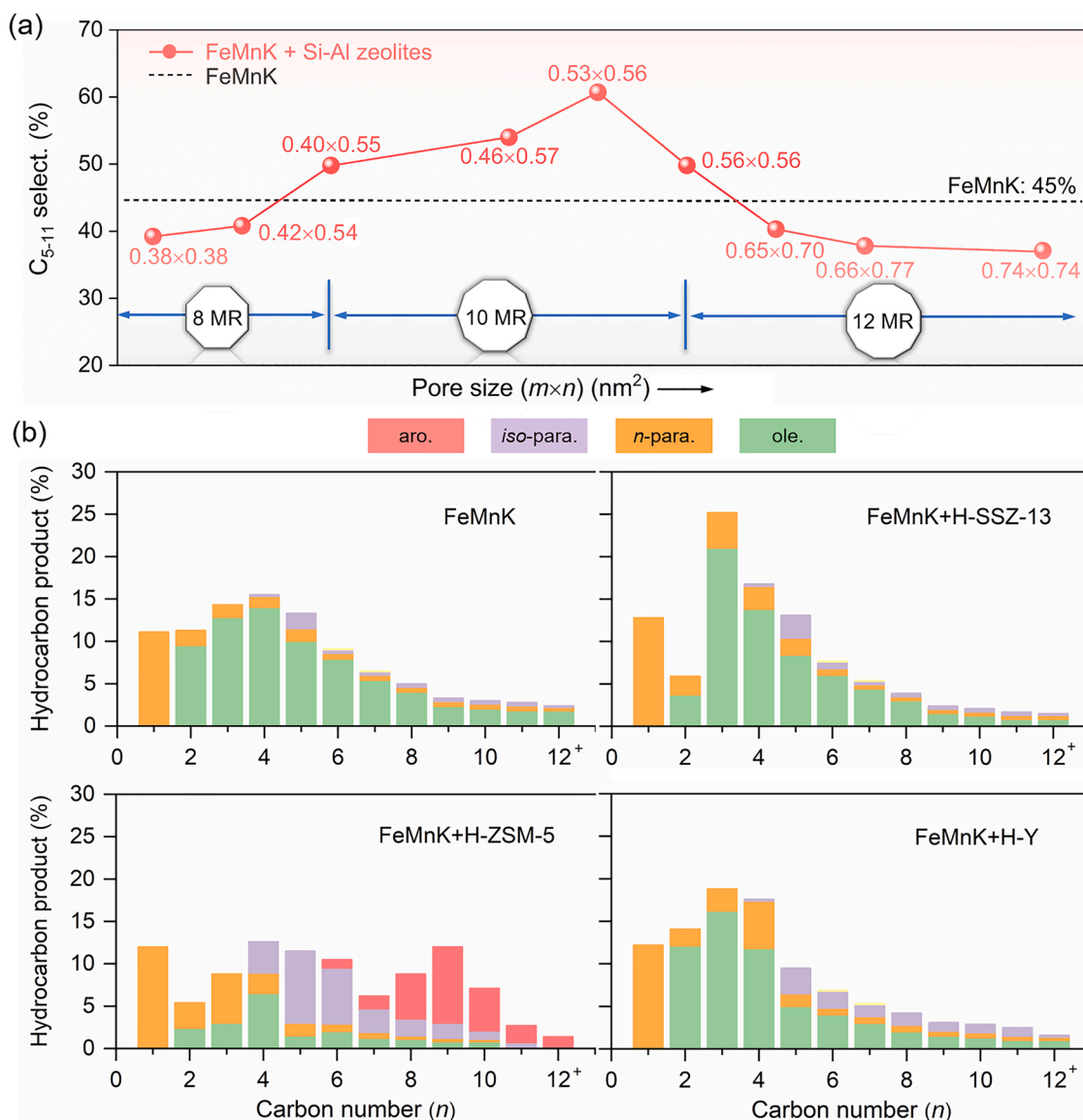
Fig. 6. (a) Effect of pore size of zeolites on the C_5–C_{11} selectivity of bifunctional FeMnK+zeolite catalysts in CO_2 hydrogenation. The pore size of Si-Al zeolites was marked in the figure. (b) The product distribution of FeMnK, FeMnK+H-SSZ-13, FeMnK+H-ZSM-5, and FeMnK+H-Y catalysts. Details for catalytic performance and reaction conditions can be found in Table S9.

SSZ-13, FeMnK+H-ZSM-5, and FeMnK+H-Y catalysts was carefully classified into aromatics, *iso*-paraffins, *n*-paraffins, and olefins (Fig. 6b). The selectivity of CH_4 was similar (11–13%) over the four catalysts. The product over FeMnK was mainly for C_{2+} α-olefins with a total selectivity of 73% (Table S3), showing a unimodal distribution with the peak at C_4 hydrocarbons. The selectivity of ethylene was lower than those of propylene and butene over FeMnK+H-SSZ-13. Compared to FeMnK, the decrease of ethylene and the increase of propylene over FeMnK+H-SSZ-13 indicated that ethylene was preferentially covered in the pores of H-SSZ-13, but most was catalyzed into propylene. The product over FeMnK+H-ZSM-5 with 10MR micropores appeared a bimodal distribution with peaks at C_4 and C_9 hydrocarbons. Compared to FeMnK and FeMnK+H-SSZ-13, the decrease of C_2–$C_4^=$ and the increase of C_5–C_{11} hydrocarbons were obvious over FeMnK+H-ZSM-5. Besides, C_5–C_{11} hydrocarbons mainly consisted of C_5–C_7 *iso*-paraffins and C_8–C_{12} aromatics (Fig. 6b), which was evidence of the olefin oligomerization, isomerization, and aromatization. Kinetically, it is easier for *iso*-paraffins and aromatics to form inside and escape from the pores of H-ZSM-5 than H-SSZ-13, owing to the shape catalysis of zeolites. The combination with larger 12MR zeolites did not affect the product distribution, mainly

due to insufficient oligomerization reaction of primary products over FeMnK. The increase of C_3–C_4 hydrocarbons indicated that the acid-cracking reaction of hydrocarbons dominated the product distribution [51]. Therefore, the selectivity of C_5–C_{11} hydrocarbons slightly decreased compared to FeMnK.

3.6. Effect of integration manners

The proximity between two functional components is crucial for bifunctional catalysis [31,39]. We investigated the effect of integration manners between FeMnK and H-ZSM-5 zeolite on the performances of CO_2 hydrogenation. Three catalysts with different proximity were denoted as FeMnK‖H-ZSM-5 with dual-bed configuration, FeMnK+H-ZSM-5 with granule-mixing configuration, and FeMnK/H-ZSM-5 with powder-mixing configuration (Details in the Catalyst synthesis). Compared with pure FeMnK catalyst, the selectivity of C_5–C_{11} hydrocarbons over FeMnK‖H-ZSM-5 with the BAS density of 0.15 mmol g^{-1} significantly increased from 35% to 65%, and the selectivity of C_2–$C_4^=$ reduced from 29% to 8.1% (Fig. 7a–b and Table S17). As the proximity increased from dual-bed to granule-mixing, the CO_2
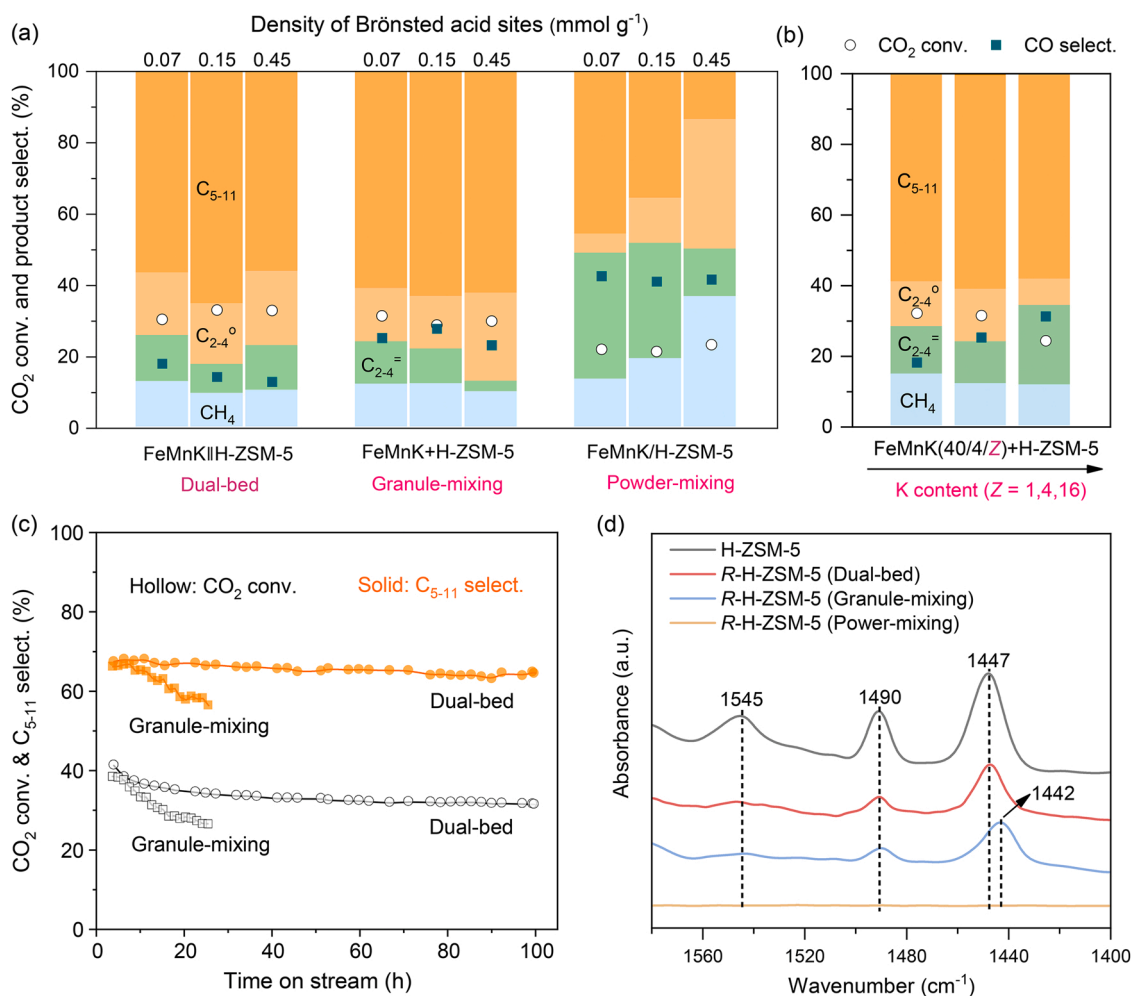
Fig. 7. (a) The effects of integration manners between FeMnK and H-ZSM-5 and acid density of H-ZSM-5 on the catalytic performance of CO_2 hydrogenation. (b) The effect of K content on the performance of FeMnK+H-ZSM-5 catalysts in CO_2 hydrogenation. (c) The stability of bifunctional catalysts composed of FeMnK and H-ZSM-5 with dual-bed and granule-mixing configurations. (d) Py-FTIR patterns of fresh or reacted H-ZSM-5 zeolites. H-ZSM-5, *R*-H-ZSM-5 (granule mixing), and *R*-H-ZSM-5 (powder mixing) represented the fresh, reacted H-ZSM-5 with granule mixing, and powder mixing after 10 h of reaction, respectively. Reaction conditions: W_{cat} = 0.30 g, T = 320 °C, P = 3 MPa, H_2/CO_2 = 3:1. Detailed catalytic performance and reaction conditions can be found in Tables S17 and S19.

conversion levels and product distributions did not change significantly and were independent of the BAS density of H-ZSM-5 (Table S17). The selectivity of CH_4 was around 10%, which was attributed to the promotion of K. The selectivity of C_5–C_{11} hydrocarbons was around 60%, thanks to the chain propagation over H-ZSM-5. Although the two functional components were not closely integrated at the nanoscale, they could well catalyze the relay conversion of CO_2 to liquid fuels.

Further increasing the proximity was detrimental to both CO_2 conversion and the selectivity of C_5–C_{11}. With the BAS density of H-ZSM-5 zeolite increasing to 0.45 mmol g^{-1}, the selectivity of CH_4 and C_2–C_4^0 all sharply increased to 36%. This performance was close to those of pure FeMn (10/4) oxide (Table S3 and S17), indicating that H-ZSM-5 and K lost their functions in gearing production distribution over bifunctional catalysts. We also compared the performance of FeMnK(10/4/4)/H-ZSM-5 and FeMn(40/4)/H-ZSM-5 with powder-mixing configuration and found that the main products were CH_4 and C_2–C_4^0 over both the two catalysts (Table S18). Overall, with the increase in the proximity of the active sites and K content, CO_2 conversion reduced but CO selectivity increased (Figs. 7a and 7b).

The performances of the dual-bed and granule-mixing configurations at the initial stage were similar, regardless of the BAS density of H-ZSM-5 (Fig. 7a). FeMnK‖H-ZSM-5 exhibited a stable C_5–C_{11} selectivity of 65%, and CO_2 conversion of about 32% after 100 h of reaction. However, the FeMnK+H-ZSM-5 catalyst deactivated quickly within

25 h of the reaction (Fig. 7c). Based on the above, we could speculate that the BAS of H-ZSM-5 was neutralized by the migration of K from FeMnK to the protonic sites of H-ZSM-5, which could be accelerated by high reaction temperature and close contact between metal and zeolite [52].

To investigate the optimum integration method, Py-FTIR was performed to probe the evolution of zeolite acidity during the reaction (Fig. 7d). Except for *R*-H-ZSM-5 (Powder-mixing), both *R*-H-ZSM-5 (Dual-bed) and *R*-H-ZSM-5 (Granule-mixing) were separated from the reacted bifunctional catalysts after 10 h. The bands at 1545 cm^{-1} and 1447 cm^{-1} can be assigned to Brønsted and Lewis acid sites (BAS and LAS) of H-ZSM-5 zeolite, respectively. The bands at 1490 cm^{-1} can be assigned to the combination of Brønsted and Lewis acid sites of H-ZSM-5 zeolite [73]. The intensity of both BAS and LAS of *R*-H-ZSM-5 (Dual-bed) became weaker compared to the fresh H-ZSM-5, mainly due to the carbon deposition of H-ZSM-5 zeolite. The intensity of LAS of *R*-H-ZSM-5 (Dual-bed) and *R*-H-ZSM-5 (Granule-mixing) was similar, but an additional peak at 1442 cm^{-1} was observed over *R*-H-ZSM-5 (Granule-mixing), suggesting that a fraction of BAS was poisoned by K^+ [74]. Since the FeMnK+H-ZSM-5 has a contact interface between granules, we can speculate that the K^+ on FeMnK oxide could migrate to BAS of H-ZSM-5 through this interface. The peaks belonging to acidic sites were almost negligible over *R*-FeMnK/H-ZSM-5 (Fig. 7d), indicating severe interaction between FeMnK and H-ZSM-5. In this case, the detrimental effect

brought by mixing two functional components closely cannot be ascribed to proximity factors but to chemical interaction or incompatibility.

TG and GC-MS analysis were performed to investigate the coke content and species of the reacted H-ZSM-5 zeolites, respectively (Fig. S11). It was observed that the coke content of H-ZSM-5 zeolites after 50 h of reaction was around 3% (Fig. S11a). Besides, the carbonaceous compounds retained in the reacted zeolites are very similar (poly-branched aromatic hydrocarbons) (Fig. S11b), indicating that the integration manners between FeMnK and H-ZSM-5 zeolite exhibited a minor impact on the coke content and species. Therefore, other than catalyst coking, the K^+ migration into H-ZSM-5 is another reason for the deactivation of FeMnK+H-ZSM-5 catalysts.

In summary, if FeMnK and H-ZSM-5 zeolite were integrated with a contact interface, K^+ on FeMnK could migrate to the BAS of H-ZSM-5 with a great inclination (Fig. 8). The degree of K^+ migration was determined by the proximity between the active sites. Since no K^+ was observed over H-ZSM-5 separated from the dual-bed configuration after the reaction, the migration of K^+ should follow an ion exchange mechanism, not gaseous diffusion. Even the granule-mixing configuration with a small interface between FeMnK and H-ZSM-5, BAS of H-ZSM-5 would be poisoned. If the FeMnK and H-ZSM-5 were closely integrated by the powder-mixing method, the K^+ could fast neutralize the BAS at the initial stage of the reaction. Moreover, the close integration may also induce the formation of Fe/Mn silicates or aluminates [75], leading to decreased CO_2 conversion and uncontrollable product distribution. Consequently, both CO_2 conversion and the selectivity of C_5–C_{11} decreased while the selectivity of CH_4 increased over the bifunctional catalysts.

3.7. Phase evolution of Fe species

It is widely accepted that Fe_3O_4 is the active site for RWGS and Fe_xC is responsible for the FT reaction over Fe-based catalysts in CO_2 hydrogenation [39,76]. The pre-reduction and reaction may induce severe evolution of Fe species, causing different catalytic behaviors [77,78].

The H_2-TPR experiment was applied to investigate the reducibility of the catalysts. The addition of K could facilitate the formation of Fe_3O_4 by the analysis of XRD (Fig. 3b). Theoretically, Fe_3O_4 consumed less hydrogen than Fe_2O_3 when the mass was the same. Therefore, the amount of hydrogen consumption for FeK and FeMnK was lower than that of Fe_2O_3, matching the calculation by H_2-TPR profiles (Table S20).

For the pristine Fe_2O_3, two obvious reduction peaks at 390 °C and 670 °C were observed (Fig. 9a), assigning to the reduction of α-Fe_2O_3 to Fe_3O_4 and Fe_3O_4 to metallic Fe, respectively [47,79]. For the FeMn oxide, the introduction of Mn slightly retarded the reduction of iron oxide [55]. However, the reduction of Fe species over the FeK oxide shifted to a lower temperature (Fig. 9a), suggesting that the introduction of K facilitated the reduction of Fe species. An additional minor H_2 consumption peak around 285 °C was observed for the FeMnK oxide, probably due to the easier reducibility of Mn^{3+} than Fe^{3+} [56]. The third reduction peak at 530 °C was assigned to the reduction from Fe_3O_4 to FeO (Fig. 9a). As an intermediate phase, FeO was presented in the reduction process of FeMnK oxides with high Mn content, which may be due to the stabilization effect of the Mn element on the Fe^{2+} species [55]. Although the Fe-based oxides were almost completely reduced to metallic Fe in H_2 for 2 h (Fig. S12), the intrinsic reducibility of the catalysts affected the carbonization of iron in the CO_2 hydrogenation (Fig. 9a). The reduced catalysts could be re-oxidized by CO_2 and formed H_2O to lead to the coexistence of iron oxides and iron carbides [80].

We performed CO_2-TPD to investigate the CO_2 adsorption capacity of the catalysts. The capacity of CO_2 adsorption was not strictly in line with the BET surface area of these oxides (Table S20), suggesting the appearance of the chemisorption of CO_2 with the addition of K and Mn promoters (Fig. 9b). Mn could promote CO_2 adsorption capacity to some extent, but its promotion was not as significant as that of K promoter. The capacity of CO_2 adsorption further increased with the co-promotion of K and Mn simultaneously. Besides, with the addition of Mn and K, the peak position shifted to higher temperatures, indicating an increase in the strength of CO_2 adsorption over FeMnK (Table S20). The higher adsorption capacity of CO_2 over Fe-based catalysts not only facilitated the formation of iron carbides through CO_2 dissociation and diffusion of C atoms into the lattice of the Fe phase but also increased the C/H ratio on the catalyst surface, which could contribute to the formation of C_2–$C_4^=$ and C_{5+} hydrocarbons [81,82].

To investigate the phase evolution of Fe species in CO_2 hydrogenation, we measured the reacted catalysts after 50 h of reaction by XRD, Mössbauer spectra, and TEM techniques. The main phase of Fe species was Fe_3O_4 over R-Fe_2O_3 catalysts without K and Mn promotes (Fig. S13). Three types of Fe species were detected in the R-Fe_2O_3 catalyst, with Fe_5C_2 accounting for 24.2%, Fe_3O_4 for 72.6%, and Fe_2O_3 for 3.2% (Fig. 10a and Table S21). With a small amount of Mn promoter, the content of Fe_5C_2 slightly increased to 38.1%, accompanied by 8.6% of Fe_7C_3 over the R-FeMn catalyst (Fig. 10b). With the promotion of K and
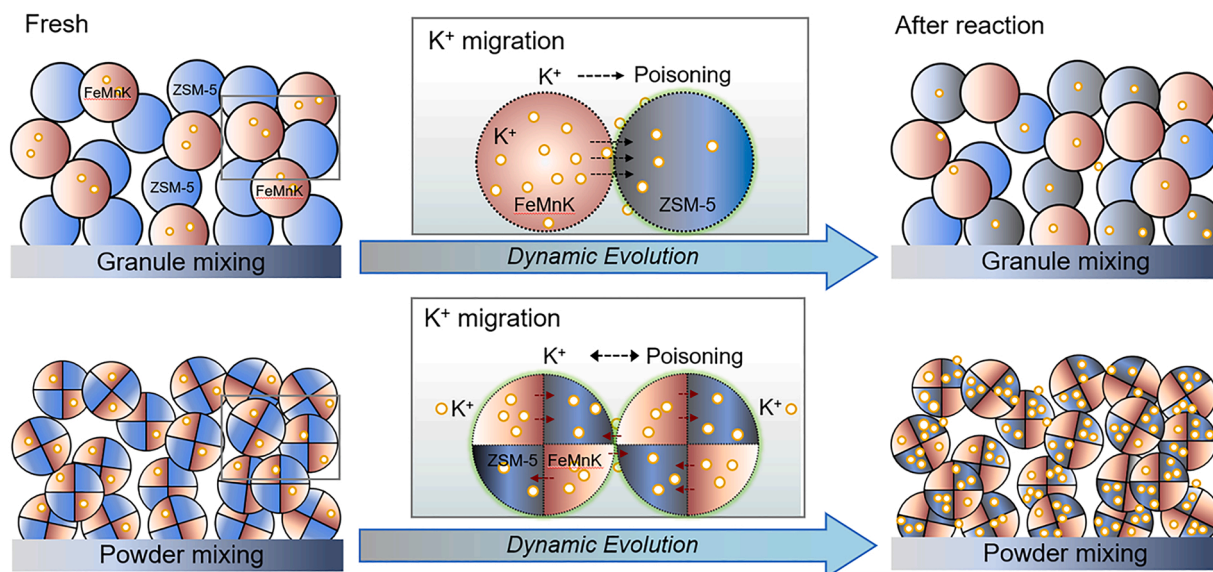

Fig. 8. Scheme of the effect of integration manners between FeMnK and H-ZSM-5 on the K^+ migration over the catalysts.
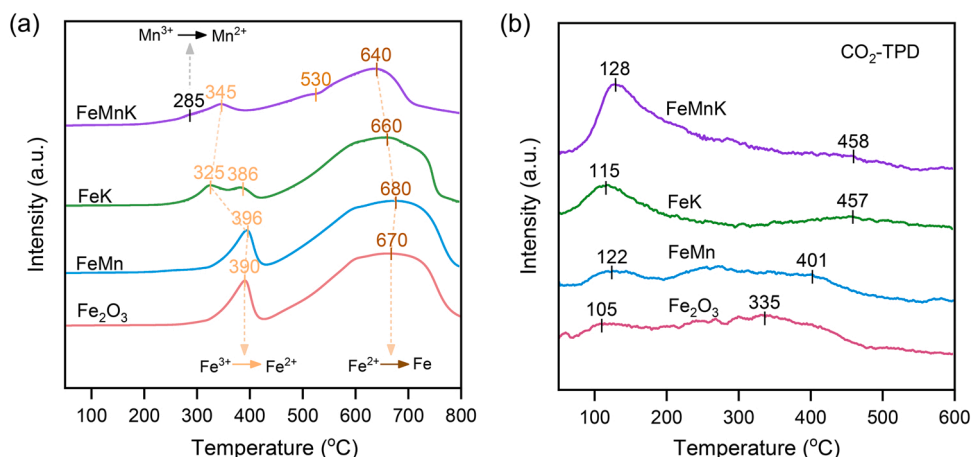
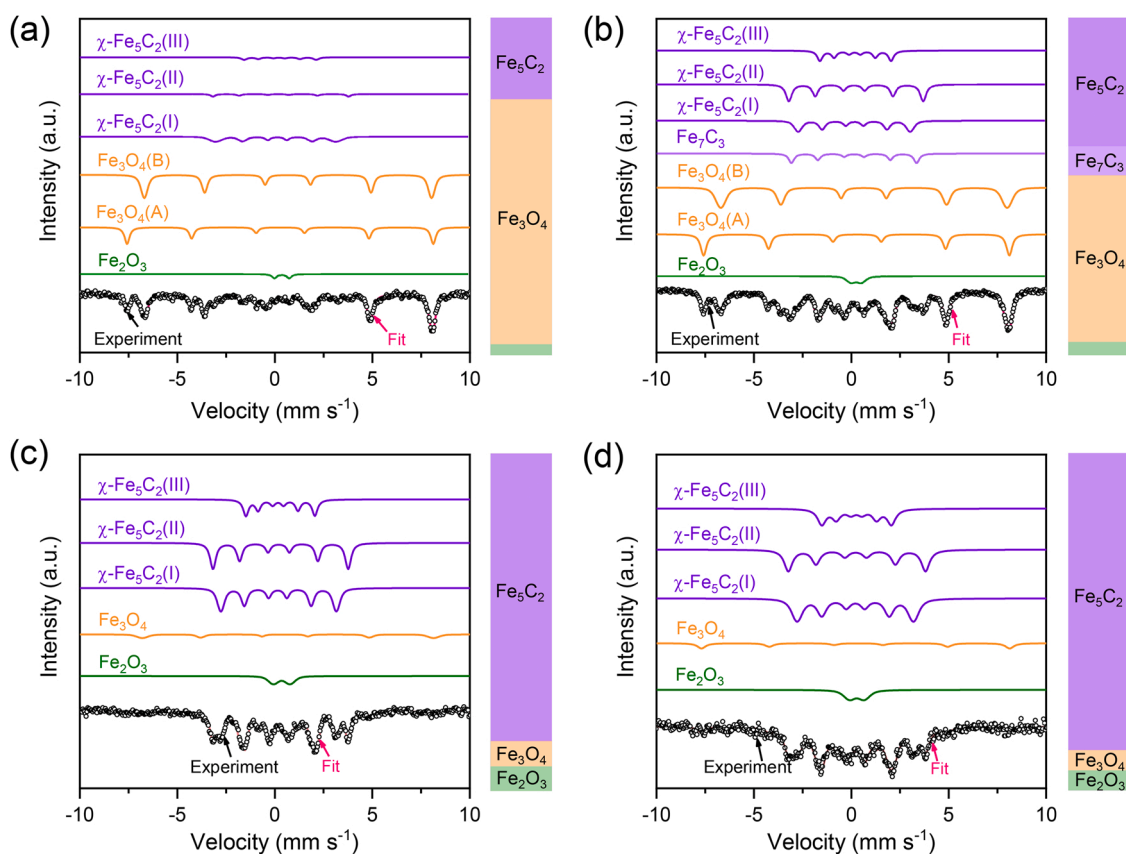**Fig. 9.** (a) H_2-TPR profiles of Fe-based catalysts and (b) CO_2-TPD profiles for their reduced forms.

Fig. 10. Mössbauer spectra of (a) R-Fe$_2$O$_3$, (b) R-FeMn, (c) R-FeMnK, and (d) R-FeMnK^{400} catalysts after 50 h of the reaction. R-catalyst^{400} represented the reacted catalyst at 400 °C after 50 h of reaction. Other catalysts were evaluated in CO_2 conversion at 320 °C.

Mn simultaneously, the content of Fe$_5$C$_2$ significantly increased to more than 85% over catalysts after the reaction either at 320 °C or 400 °C (Fig. 10c–d). TEM images confirmed that the morphology of the catalyst also changed after 50 h of reaction. The fresh FeMnK consisted of the nanospheres with an average particle size of 10 nm, while the core-shell structures were formed over R-FeMnK catalyst, composed of Fe$_3$O$_4$ core (diameter from 50 nm to 80 nm) and Fe$_5$C$_2$ shell (thickness of 5 nm) (Fig. 11). This core-shell structure was also confirmed by Guo and co-workers [83].

Based on the above, the phase evolution of Fe species in CO_2 hydrogenation becomes clear. The Fe oxides were first reduced to their

metallic state after H_2 activation. Subsequently, a mixture of Fe$_3$O$_4$ and Fe$_5$C$_2$ formed in CO_2 hydrogenation, responsible for RWGS and the FT reaction, respectively. The composition of Fe$_3$O$_4$ and Fe$_5$C$_2$ was associated with the interaction of metallic Fe with carbon and oxygen species from the dissociated CO_2. With the promotion of K and Mn simultaneously, both the reducibility and CO_2 adsorption capacity of the catalysts could be enhanced, contributing to the phase transformation from Fe species to Fe$_5$C$_2$. This could be the reason that the optimum selectivity of both C$_2$–C$_4^=$ and C$_{5+}$ hydrocarbons was obtained over the FeMnK catalyst.
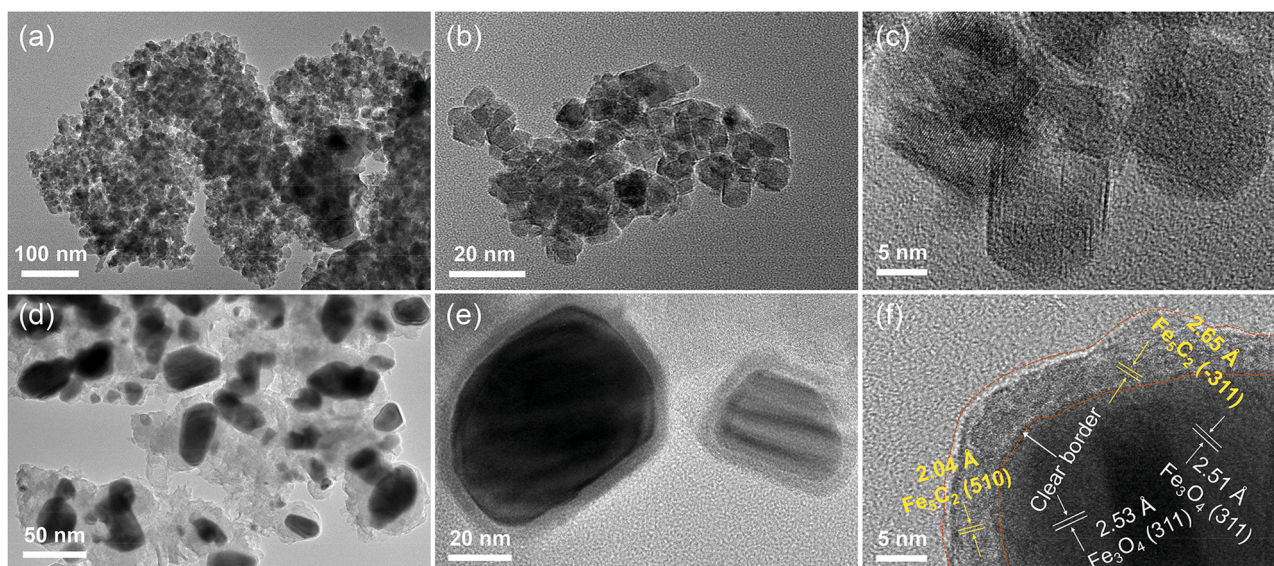
Fig. 11. TEM images of the (a, b, c) fresh FeMnK and (d, e, f) *R*-FeMnK catalysts after 50 h of reaction.

3.8. Reaction mechanism

The results obtained in the present work allow us to propose the reaction mechanism for CO_2 hydrogenation over FeMnK-zeolite bifunctional catalysts (Fig. 12). A Fe_3O_4 @Fe_5C_2 core-shell structure was observed over the FeMnK catalyst in CO_2 hydrogenation. CO_2 is first converted to CO via RWGS reaction on Fe_3O_4 sites, and then CO is hydrogenated to C_{2+} olefins with a selectivity of 73% via FT reaction on Fe_5C_2 sites. The C_{2+} olefins subsequently diffuse into micropores of 10MR zeolites and undergo oligomerization into C_{5+} olefins on BAS, which can be further transformed into aromatics via cyclization and dehydrogenation or *iso*-paraffins via isomerization. In particular, C_5–C_{11} hydrocarbons with a selectivity of 70% can be obtained over the FeMnK+H-ZSM-5 catalyst. The formation of C_5–C_{11} hydrocarbons in zeolite channels is shape-selective, and only the zeolites with 10MR micropores could promote the C_5–C_{11} selectivity in CO_2 hydrogenation. Although C_2H_4 could be converted in the 8MR micropores, only the formation of C_3H_6 was enhanced due to the pore size restriction. The combination with larger 12MR zeolites slightly affects the distribution of primary products on FeMnK, mainly due to the insufficient oligomerization ability of C_{2+} olefins. The olefin oligomerization is a key step for

the further increment of C_5–C_{11} selectivity over FeMnK-zeolites. It is noteworthy that the alkaline metals can easily migrate to the protonic sites of zeolites and neutralize BAS, thus the integration between FeMnK and H-ZSM-5 with a proper distance must be ensured.

4. Conclusion

The bifunctional catalysts, composed of FeMnK oxide and nine zeolites with different topologies, have been investigated for CO_2 hydrogenation at high temperatures. FeMnK+H-ZSM-5 offered a 70% selectivity of C_5–C_{11} hydrocarbons together with a 17% selectivity of C_2–C_4 olefins. A volcano trend was obtained between the pore size of zeolites and the selectivity of C_5–C_{11} hydrocarbons. The 10MR zeolites favored the formation of C_5–C_{11} hydrocarbons, while both 8MR and 12MR zeolites could not promote the C–C chain growth. As the temperature increased from 320 °C to 400 °C, CO_2 conversion increased significantly from 32% to 51% while CO selectivity was kept at low levels of around 15%. Besides, the yield of aromatics increased more than doubled over the FeMnK+H-ZSM-5 catalyst. The effects of integration manners between FeMnK and H-ZSM-5 on the performances of CO_2 hydrogenation were carefully investigated. If FeMnK and H-ZSM-5
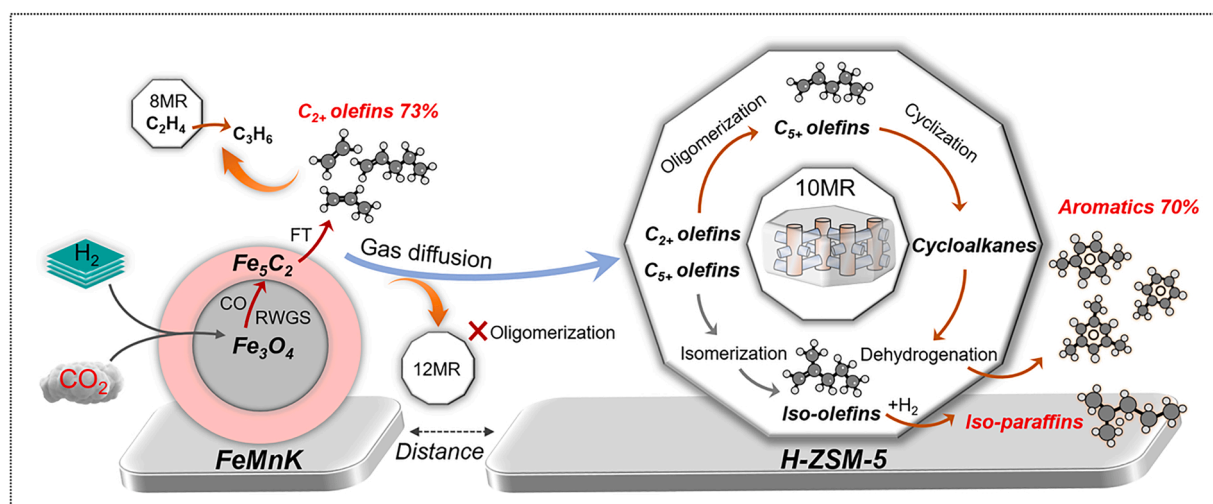

Fig. 12. Reaction mechanism for CO_2 hydrogenation over FeMnK+zeolite bifunctional catalysts.

were integrated with a contact interface, K^+ would migrate to H-ZSM-5 and neutralize the BAS, following an ion exchange mechanism. The degree of K^+ migration depended on the proximity between the active sites and the separation of two components could prevent the migration of K^+ ions. Without the disturbance of K^+, the H-ZSM-5 could well catalyze the olefin oligomerization, isomerization, cyclization, and aromatization. This work not only benefits the precise design of high-temperature catalysts for CO_2 hydrogenation into liquid fuels and chemicals but also demonstrates the potential to couple green hydrogen for CO_2 upcycling.

CRediT authorship contribution statement

Yubing Li: Data curation, Visualization, Roles/Writing - original draft. **Lei Zeng:** Data curation, Investigation, Experiment. **Ge Pang:** Data curation, Catalyst evaluation. **Xueer Wei:** Catalyst characterization. **Mengheng Wang:** Catalyst evaluation, Data analysis, Visualization, Writing - review & editing. **Kang Cheng:** Conceptualization, Data analysis, Writing - review & editing. **Jincan Kang:** Formal analysis, Investigation. **José M. Serra:** Supervision, Project administration. **Qinghong Zhang:** Methodology, Writing - review & editing, Funding acquisition. **Ye Wang:** Supervision, Data analysis.

Declaration of Competing Interest

The authors declare that they have no known competing financial interests or personal relationships that could have appeared to influence the work reported in this paper.

Data Availability

Data will be made available on request.

Acknowledgments

Appendix A. Supporting information

Supplementary data associated with this article can be found in the online version at doi:10.1016/j.apcatb.2022.122299.

References

[1] S.K. Kim, J. Shin, S.I. An, H.J. Kim, N. Im, S.-P. Xie, J.-S. Kug, S.-W. Yeh, Widespread irreversible changes in surface temperature and precipitation in response to CO_2 forcing, Nat. Clim. Change 12 (2022) 834–840.

[2] Y. Ou, C. Roney, J. Alsalam, K. Calvin, J. Creason, J. Edmonds, A.A. Fawcett, P. Kyle, K. Narayan, P. O'Rourke, P. Patel, S. Ragnauth, S.J. Smith, H. McJeon, Deep mitigation of CO_2 and non-CO_2 greenhouse gases toward 1.5 degrees C and 2 degrees C futures, Nat. Commun. 12 (2021) 6245.

[3] G. Singh, J. Lee, A. Karakoti, R. Bahadur, J. Yi, D. Zhao, K. AlBahily, A. Vinu, Emerging trends in porous materials for CO_2 capture and conversion, Chem. Soc. Rev. 49 (2020) 4360–4404.

[4] M.D. Garba, M. Usman, S. Khan, F. Shehzad, A. Galadima, M.F. Ehsan, A. S. Ghanem, M. Humayun, CO_2 towards fuels: a review of catalytic conversion of carbon dioxide to hydrocarbons, J. Environ. Chem. Eng. 9 (2021) 104756.

[5] A. Alvarez, A. Bansode, A. Urakawa, A.V. Bavykina, T.A. Wezendonk, M. Makkee, J. Gascon, F. Kapteijn, Challenges in the greener production of formates/formic acid, methanol, and DME by heterogeneously catalyzed CO_2 hydrogenation processes, Chem. Rev. 117 (2017) 9804–9838.

[6] H. Shin, K.U. Hansen, F. Jiao, Techno-economic assessment of low-temperature carbon dioxide electrolysis, Nat. Sustain. 4 (2021) 911–919.

[7] X. Jiang, X. Nie, X. Guo, C. Song, J.G. Chen, Recent advances in carbon dioxide hydrogenation to methanol via heterogeneous catalysis, Chem. Rev. 120 (2020) 7984–8034.

[8] I.A. Digdaya, I. Sullivan, M. Lin, L. Han, W.H. Cheng, H.A. Atwater, C. Xiang, A direct coupled electrochemical system for capture and conversion of CO_2 from oceanwater, Nat. Commun. 11 (2020) 4412.

[9] P. Gao, L. Zhong, B. Han, M. He, Y. Sun, Green carbon science: keeping the pace in practice, Angew. Chem. Int. Ed. (2022) e202210095.

[10] F. Zeng, C. Mebrahtu, X. Xi, L. Liao, J. Ren, X. Xie, H.J. Heeres, R. Palkovits, Catalysts design for higher alcohols synthesis by CO_2 hydrogenation: Trends and future perspectives, Appl. Catal. B Environ. 291 (2021) 120073.

[11] T.N. Do, C. You, J. Kim, A CO2 Utilization framework for liquid fuels and chemical production: techno-economic and environmental analysis, Energy Environ. Sci. 15 (2022) 169–184.

[12] P. Gao, L. Zhang, S. Li, Z. Zhou, Y. Sun, Novel heterogeneous catalysts for CO_2 hydrogenation to liquid fuels, ACS Cent. Sci. 6 (2020) 1657–1670.

[13] M. Aresta, A. Dibenedetto, A. Angelini, Catalysis for the valorization of exhaust carbon: from CO_2 to chemicals, materials, and fuels. technological use of CO_2, Chem. Rev. 114 (2014) 1709–1742.

[14] S. Xie, W. Ma, X. Wu, H. Zhang, Q. Zhang, Y. Wang, Y. Wang, Photocatalytic and electrocatalytic transformations of C1 molecules involving C–C coupling, Energy Environ. Sci. 14 (2021) 37–89.

[15] Y. Jiang, R. Long, Y. Xiong, Regulating C–C coupling in thermocatalytic and electrocatalytic CO_x conversion based on surface science, Chem. Sci. 10 (2019) 7310–7326.

[16] B.M. Tackett, E. Gomez, J.G. Chen, Net reduction of CO_2 via its thermocatalytic and electrocatalytic transformation reactions in standard and hybrid processes, Nat. Catal. 2 (2019) 381–386.

[17] C. Zhou, J. Shi, W. Zhou, K. Cheng, Q. Zhang, J. Kang, Y. Wang, Highly active ZnO-ZrO₂ aerogels integrated with H-ZSM-5 for aromatics synthesis from carbon dioxide, ACS Catal. 10 (2020) 302–310.

[18] M.T. Arslan, G. Tian, B. Ali, C. Zhang, H. Xiong, Z. Li, L. Luo, X. Chen, F. Wei, Highly selective conversion of CO_2 or CO into precursors for kerosene-based aviation fuel via an aldol–aromatic mechanism, ACS Catal. 12 (2022) 2023–2033.

[19] L. Zhang, Y. Dang, X. Zhou, P. Gao, A. Petrus van Bavel, H. Wang, S. Li, L. Shi, Y. Yang, E.I. Vovk, Y. Gao, Y. Sun, Direct conversion of CO_2 to a jet fuel over CoFe alloy catalysts, Innov. (Camb.) 2 (2021) 100170.

[20] A. Dokania, S. Ould-Chikh, A. Ramirez, J.L. Cerrillo, A. Aguilar, A. Russkikh, A. Alkhalaf, I. Hita, A. Bavykina, G. Shterk, N. Wehbe, A. Prat, E. Lahera, P. Castano, E. Fonda, J.L. Hazemann, J. Gascon, Designing a multifunctional catalyst for the direct production of gasoline-range isoparaffins from CO_2, JACS Au 1 (2021) 1961–1974.

[21] R.P. Ye, J. Ding, W. Gong, M.D. Argyle, Q. Zhong, Y. Wang, C.K. Russell, Z. Xu, A. G. Russell, Q. Li, M. Fan, Y.G. Yao, CO_2 hydrogenation to high-value products via heterogeneous catalysis, Nat. Commun. 10 (2019) 5698.

[22] A. Hauch, R. Kungas, P. Blennow, A.B. Hansen, J.B. Hansen, B.V. Mathiesen, M. B. Mogensen, Recent advances in solid oxide cell technology for electrolysis, Science 370 (2020) 186.

[23] E.C. Ra, K.Y. Kim, E.H. Kim, H. Lee, K. An, J.S. Lee, Recycling carbon dioxide through catalytic hydrogenation: recent key developments and perspectives, ACS Catal. 10 (2020) 11318–11345.

[24] P. Bains, P. Psarras, J. Wilcox, CO_2 capture from the industry sector, Prog. Energy Combust. 63 (2017) 146–172.

[25] J. Wang, G. Li, Z. Li, C. Tang, Z. Feng, H. An, H. Liu, T. Liu, C. Li, A highly selective and stable ZnO-ZrO₂ solid solution catalyst for CO_2 hydrogenation to methanol, Sci. Adv. 3 (2017), e1701290.

[26] J. Hu, L. Yu, J. Deng, Y. Wang, K. Cheng, C. Ma, Q. Zhang, W. Wen, S. Yu, Y. Pan, J. Yang, H. Ma, F. Qi, Y. Wang, Y. Zheng, M. Chen, R. Huang, S. Zhang, Z. Zhao, J. Mao, X. Meng, Q. Ji, G. Hou, X. Han, X. Bao, Y. Wang, D. Deng, Sulfur vacancy-rich MoS₂ as a catalyst for the hydrogenation of CO_2 to methanol, Nat. Catal. 4 (2021) 242–250.

[27] C. Liu, J. Kang, Z.Q. Huang, Y.H. Song, Y.S. Xiao, J. Song, J.X. He, C.R. Chang, H. Q. Ge, Y. Wang, Z.T. Liu, Z.W. Liu, Gallium nitride catalyzed the direct hydrogenation of carbon dioxide to dimethyl ether as primary product, Nat. Commun. 12 (2021) 2305.

[28] J.I. Orege, J. Wei, Y. Han, M. Yang, X. Sun, J. Zhang, C.C. Amoo, Q. Ge, J. Sun, Highly stable Sr and Na co-decorated Fe catalyst for high-valued olefin synthesis from CO_2 hydrogenation, Appl. Catal. B: Environ. 316 (2022) 121640.

[29] Y. Lou, F. jiang, W. Zhu, L. Wang, T. Yao, S. Wang, B. Yang, B. Yang, Y. Zhu, X. Liu, CeO₂ supported Pd dimers boosting CO_2 hydrogenation to ethanol, Appl. Catal. B: Environ. 291 (2021) 120122.

[30] P. Gao, S. Li, X. Bu, S. Dang, Z. Liu, H. Wang, L. Zhong, M. Qiu, C. Yang, J. Cai, W. Wei, Y. Sun, Direct conversion of CO_2 into liquid fuels with high selectivity over a bifunctional catalyst, Nat. Chem. 9 (2017) 1019–1024.

[31] F. Jiao, J. Li, X. Pan, J. Xiao, H. Li, H. Ma, M. Wei, Y. Pan, Z. Zhou, M. Li, S. Miao, J. Li, Y. Zhu, D. Xiao, T. He, J. Yang, F. Qi, D. Fu, X. Bao, Selective conversion of syngas to light olefins, Science 351 (2016) 1065–1068.

[32] K. Cheng, B. Gu, X. Liu, J. Kang, Q. Zhang, Y. Wang, Direct and highly selective conversion of synthesis gas into lower olefins: design of a bifunctional catalyst combining methanol synthesis and carbon-carbon coupling, Chem. Int. 55 (2016) 4725–4728.

[33] W. Zhou, K. Cheng, J. Kang, C. Zhou, V. Subramanian, Q. Zhang, Y. Wang, New horizon in C1 chemistry: breaking the selectivity limitation in transformation of syngas and hydrogenation of CO_2 into hydrocarbon chemicals and fuels, Chem. Soc. Rev. 48 (2019) 3193–3228.

[34] X. Liu, W. Zhou, Y. Yang, K. Cheng, J. Kang, L. Zhang, G. Zhang, X. Min, Q. Zhang, Y. Wang, Design of efficient bifunctional catalysts for direct conversion of syngas into lower olefins via methanol/dimethyl ether intermediates, Chem. Sci. 9 (2018) 4708–4718.

[35] S. Wang, L. Zhang, P. Wang, X. Liu, Y. Chen, Z. Qin, M. Dong, J. Wang, L. He, U. Olsbye, W. Fan, Highly effective conversion of CO₂ into light olefins abundant in ethene, Chem 8 (2022) 1376–1394.

[36] J. Wei, R. Yao, Y. Han, Q. Ge, J. Sun, Towards the development of the emerging process of CO₂ heterogenous hydrogenation into high-value unsaturated heavy hydrocarbons, Chem. Soc. Rev. 50 (2021) 10764–10805.

[37] Y. Wang, L. Tan, M. Tan, P. Zhang, Y. Fang, Y. Yoneyama, G. Yang, N. Tsubaki, Rationally designing bifunctional catalysts as an efficient strategy to boost CO₂ hydrogenation producing value-added aromatics, ACS Catal. 9 (2019) 895–901.

[38] J. Wei, R. Yao, Q. Ge, D. Xu, C. Fang, J. Zhang, H. Xu, J. Sun, Precisely regulating Brønsted acid sites to promote the synthesis of light aromatics via CO₂ hydrogenation, Appl. Catal. B: Environ. 283 (2021), 119648.

[39] J. Wei, Q. Ge, R. Yao, Z. Wen, C. Fang, L. Guo, H. Xu, J. Sun, Directly converting CO₂ into a gasoline fuel, Nat. Commun. 8 (2017) 15174.

[40] X. Cui, P. Gao, S. Li, C. Yang, Z. Liu, H. Wang, L. Zhong, Y. Sun, Selective production of aromatics directly from carbon dioxide hydrogenation, ACS Catal. 9 (2019) 3866–3876.

[41] A. Ramirez, X. Gong, M. Caglayan, S.F. Nastase, E. Abou-Hamad, L. Gevers, L. Cavallo, A. Dutta Chowdhury, J. Gascon, Selectivity descriptors for the direct hydrogenation of CO₂ to hydrocarbons during zeolite-mediated bifunctional catalysis, Nat. Commun. 12 (2021) 5914.

[42] J. Kang, K. Cheng, L. Zhang, Q. Zhang, J. Ding, W. Hua, Y. Lou, Q. Zhai, Y. Wang, Mesoporous zeolite-supported ruthenium nanoparticles as highly selective fischer–tropsch catalysts for the production of C₅–C₁₁ isoparaffins, Angew. Chem. Int. Ed. 50 (2011) 5200–5203.

[43] K. Cheng, W. Zhou, J. Kang, S. He, S. Shi, Q. Zhang, Y. Pan, W. Wen, Y. Wang, Bifunctional catalysts for one-step conversion of syngas into aromatics with excellent selectivity and stability, Chem 3 (2017) 334–347.

[44] P. Gao, S. Li, X. Bu, S. Dang, Z. Liu, H. Wang, L. Zhong, M. Qiu, C. Yang, J. Cai, W. Wei, Y. Sun, Direct conversion of CO₂ into liquid fuels with high selectivity over a bifunctional catalyst, Nat. Chem. 9 (2017) 1019–1024.

[45] Z. Li, Y. Qu, J. Wang, H. Liu, M. Li, S. Miao, C. Li, Highly selective conversion of carbon dioxide to aromatics over tandem catalysts, Joule 3 (2019) 570–583.

[46] B. Yao, T. Xiao, O.A. Makgae, X. Jie, S. Gonzalez-Cortes, S. Guan, A.I. Kirkland, J. R. Dilworth, H.A. Al-Megren, S.M. Alshihri, P.J. Dobson, G.P. Owen, J.M. Thomas, P.P. Edwards, Transforming carbon dioxide into jet fuel using an organic combustion-synthesized Fe-Mn-K catalyst, Nat. Commun. 11 (2020) 6395.

[47] Y. Xu, P. Zhai, Y. Deng, J. Xie, X. Liu, S. Wang, D. Ma, Highly selective olefin production from CO₂ hydrogenation on iron catalysts: a subtle synergy between manganese and sodium additives, Angew. Chem. Int. Ed. 59 (2020) 21736–21744.

[48] G. Song, M. Li, P. Yan, M.A. Nawaz, D. Liu, High conversion to aromatics via CO₂-FT over a CO-reduced Cu-Fe₂O₃ catalyst integrated with HZSM-5, ACS Catal. 10 (2020) 11268–11279.

[49] Y. Li, M. Wang, S. Liu, F. Wu, Q. Zhang, S. Zhang, K. Cheng, Y. Wang, Distance for communication between metal and acid sites for syngas conversion, ACS Catal. 12 (2022) 8793–8801.

[50] J. Xiao, K. Cheng, X. Xie, M. Wang, S. Xing, Y. Liu, T. Hartman, D. Fu, K. Bossers, M.A. van Huis, A. van Blaaderen, Y. Wang, B.M. Weckhuysen, Tandem catalysis with double-shelled hollow spheres, Nat. Mater. 21 (2022) 572–579.

[51] K. Cheng, L.C.J. Smulders, L.I. van der Wal, J. Oenema, J.D. Meeldijk, N.L. Visser, G. Sunley, T. Roberts, Z. Xu, E. Doskocil, H. Yoshida, Y. Zheng, J. Zecevic, P.E. de Jongh, K.P. de Jong, Maximizing noble metal utilization in solid catalysts by control of nanoparticle location, Science 377 (2022) 204–208.

[52] Y. Wang, G. Wang, L.I. van der Wal, K. Cheng, Q. Zhang, K.P. de Jong, Y. Wang, Visualizing element migration over bifunctional metal-zeolite catalysts and its impact on catalysis, Angew. Chem. Int. Ed. 60 (2021) 17735–17743.

[53] M. Wang, J. Kang, X. Xiong, F. Zhang, K. Cheng, Q. Zhang, Y. Wang, Effect of zeolite topology on the hydrocarbon distribution over bifunctional ZnAlO/SAPO catalysts in syngas conversion, Catal. Today 371 (2021) 85–92.

[54] K. Cheng, L. Zhang, J.C. Kang, X.B. Peng, Q.H. Zhang, Y. Wang, Selective transformation of syngas into gasoline-range hydrocarbons over mesoporous H-ZSM-5-supported cobalt nanoparticles, Chem. Eur. J. 21 (2015) 1928–1937.

[55] T. Li, H. Wang, Y. Yang, H. Xiang, Y. Li, Effect of manganese on the catalytic performance of an iron-manganese bimetallic catalyst for light olefin synthesis, J. Energy Chem. 22 (2013) 624–632.

[56] B. Liu, S. Geng, J. Zheng, X. Jia, F. Jiang, X. Liu, Unravelling the new roles of Na and Mn promoter in CO₂ hydrogenation over Fe₃O₄-based catalysts for enhanced selectivity to light α-olefins, ChemCatChem 10 (2018) 4718–4732.

[57] Q. Zhang, J. Yu, A. Corma, Applications of zeolites to C1 chemistry: recent advances, challenges, and opportunities, Adv. Mater. 32 (2020), e2002927.

[58] A.J. Jones, E. Iglesia, The strength of brønsted acid sites in microporous aluminosilicates, ACS Catal. 5 (2015) 5741–5755.

[59] G.V.A. Martins, G. Berlier, C. Bisio, S. Coluccia, H.O. Pastore, L. Marchese, Quantification of brønsted acid sites in microporous catalysts by a combined FTIR and NH₃-TPD study, J. Phys. Chem. C 112 (2008) 7193–7200.

[60] L. Tang, K.-G. Haw, Y. Zhang, Q. Fang, S. Qiu, V. Valtchev, Fast and efficient synthesis of SSZ-13 by interzeolite conversion of Zeolite Beta and Zeolite L, Micropor. Mesopor, Mater 280 (2019) 306–314.

[61] X. Feng, P. Zhang, Y. Fang, W. Charusiri, J. Yao, X. Gao, Q. Wei, P. Reubroycharoen, T. Vitidsant, Y. Yoneyama, G. Yang, N. Tsubaki, Designing a hierarchical nanosheet ZSM-35 zeolite to realize more efficient ethanol synthesis from dimethyl ether and syngas, Catal. Today 343 (2020) 206–214.

[62] J. Wei, R. Yao, Q. Ge, Z. Wen, X. Ji, C. Fang, J. Zhang, H. Xu, J. Sun, Catalytic hydrogenation of CO₂ to isoparaffins over Fe-based multifunctional catalysts, ACS Catal. 8 (2018) 9958–9967.

[63] S. Ferdov, Conventional synthesis of layer-like zeolites with faujasite (FAU) structure and their pathway of crystallization, Micro Mesopor. Mater. 303 (2020), 110263.

[64] S. Li, J. Li, M. Dong, S. Fan, T. Zhao, J. Wang, W. Fan, Strategies to control zeolite particle morphology, Chem. Soc. Rev. 48 (2019) 885–907.

[65] M. Zhang, Y. Chen, L. Wang, Q. Zhang, C.-W. Tsang, C. Liang, Shape selectivity in hydroisomerization of hexadecane over Pt supported on 10-Ring zeolites: ZSM-22, ZSM-23, ZSM-35, and ZSM-48, Ind. Eng. Chem. Res. 55 (2016) 6069–6078.

[66] M. Nichterwitz, S. Grätz, W. Nickel, L. Borchardt, Solvent-free hierarchization of zeolites by carbochlorination, J. Mater. Chem. A 5 (2017) 221–229.

[67] C. Wen, J. Jiang, C. Chiliu, Z. Tian, X. Xu, J. Wu, C. Wang, L. Ma, Single-step selective conversion of carbon dioxide to aromatics over Na-Fe₃O₄/Hierarchical HZSM-5 Zeolite Catalyst, Energ. Fuel 34 (2020) 11282–11289.

[68] H. Tian, H. He, J. Jiao, F. Zha, X. Guo, X. Tang, Y. Chang, Tandem catalysts composed of different morphology HZSM-5 and metal oxides for CO₂ hydrogenation to aromatics, Fuel 314 (2022), 123119.

[69] O. Muraza, Maximizing diesel production through oligomerization: a landmark opportunity for zeolite research, Ind. Eng. Chem. Res. 54 (2015) 781–789.

[70] X. Chen, M. Dong, X. Niu, K. Wang, G. Chen, W. Fan, J. Wang, Z. Qin, Influence of Zn species in HZSM-5 on ethylene aromatization, Chin. J. Catal. 36 (2015) 880–888.

[71] Y. Xu, C. Shi, B. Liu, T. Wang, J. Zheng, W. Li, D. Liu, X. Liu, Selective production of aromatics from CO₂, Catal. Sci. Technol. 9 (2019) 593–610.

[72] Y. Wang, S. Kazumi, W. Gao, X. Gao, H. Li, X. Guo, Y. Yoneyama, G. Yang, N. Tsubaki, Direct conversion of CO₂ to aromatics with high yield via a modified Fischer-Tropsch synthesis pathway, Appl. Catal. B Environ. 269 (2020), 118792.

[73] L. Rodríguez-González, F. Hermes, M. Bertmer, E. Rodríguez-Castellón, A. Jiménez-López, U. Simon, The acid properties of H-ZSM-5 as studied by NH₃-TPD and ²⁷Al-MAS NMR spectroscopy, Appl. Catal. A 328 (2007) 174–182.

[74] G. Näfe, M.A. López-Martínez, M. Dyballa, M. Hunger, Y. Traa, T. Hirth, E. Klemm, Deactivation behavior of alkali-metal zeolites in the dehydration of lactic acid to acrylic acid, J. Catal. 329 (2015) 413–424.

[75] K. Latham, C.I. Round, C.D. Williams, Synthesis, further characterisation and catalytic activity of iron-substituted zeolite LTL, prepared using tetrahedral oxoanion species, Micropororous Mesopororous Mater 38 (2000) 333–344.

[76] M.K. Khan, P. Butolia, H. Jo, M. Irshad, D. Han, K.-W. Nam, J. Kim, Selective conversion of carbon dioxide into liquid hydrocarbons and long-chain α-Olefins over Fe-amorphous AlOₓ bifunctional catalysts, ACS Catal. 10 (2020) 10325–10338.

[77] M. Ding, Y. Yang, B. Wu, Y. Li, T. Wang, L. Ma, Study on reduction and carburization behaviors of iron phases for iron-based Fischer–Tropsch synthesis catalyst, Appl. Energ. 160 (2015) 982–989.

[78] F. Gao, H. Wang, M. Qing, Y. Yang, Y. Li, Controlling the phase transformations and performance of iron-based catalysts in the Fischer-Tropsch synthesis, Chin. J. Catal. 34 (2013) 1312–1325.

[79] F. Jiang, B. Liu, S. Geng, Y. Xu, X. Liu, Hydrogenation of CO₂ into hydrocarbons: enhanced catalytic activity over Fe-based Fischer–Tropsch catalysts, Catal. Sci. Technol. 8 (2018) 4097–4107.

[80] R. Yao, J. Wei, Q. Ge, J. Xu, Y. Han, H. Xu, J. Sun, Structure sensitivity of iron oxide catalyst for CO₂ hydrogenation, Catal. Today 371 (2021) 134–141.

[81] N. Boreriboon, X. Jiang, C. Song, P. Prasassarakich, Higher hydrocarbons synthesis from CO₂ hydrogenation over K- and La-promoted Fe–Cu/TiO₂ catalysts, Top. Catal. 61 (2018) 1551–1562.

[82] J. Jiang, C. Wen, Z. Tian, Y. Wang, Y. Zhai, L. Chen, Y. Li, Q. Liu, C. Wang, L. Ma, Manganese-promoted Fe₃O₄ microsphere for efficient conversion of CO₂ to light olefins, Ind. Eng. Chem. Res. 59 (2020) 2155–2162.

[83] J. Zhu, P. Wang, X. Zhang, G. Zhang, R. Li, W. Li, T.P. Senftle, W. Liu, J. Wang, Y. Wang, A. Zhang, Q. Fu, C. Song, X. Guo, Dynamic structural evolution of iron catalysts involving competitive oxidation and carburization during CO₂ hydrogenation, Sci. Adv. 8 (2022) eabm3629.